HHS Public Access

Author manuscript

Cancer Discov. Author manuscript; available in PMC 2023 October 03.

Published in final edited form as:

Cancer Discov. 2023 April 03; 13(4): 1002–1025. doi:10.1158/2159-8290.CD-22-0805.

LKB1-dependent regulation of TPI1 creates a divergent metabolic liability between human and mouse lung adenocarcinoma

Benjamin D. Stein[1,14,*], **John R. Ferrarone**[1,14], **Eric E. Gardner**[1], **Jae Won Chang**[2,9], **David Wu**[1], **Pablo E. Hollstein**[3,10], **Roger J. Liang**[1,11], **Min Yuan**[4], **Qiuying Chen**[5], **John S. Coukos**[2], **Miriam Sindelar**[4,12], **Bryan Ngo**[1,13], **Steven S. Gross**[5], **Reuben J. Shaw**[3], **Chen Zhang**[6], **John M. Asara**[4,7], **Raymond E. Moellering**[2], **Harold Varmus**[1,*], **Lewis C. Cantley**[1,8,*]

[1]Sandra and Edward Meyer Cancer Center, Department of Medicine, Weill Cornell Medicine, New York, NY 10065, USA.

[2]Department of Chemistry, University of Chicago, Chicago, IL 60637, USA.

[3]Molecular and Cell Biology Laboratory, The Salk Institute for Biological Studies, La Jolla, CA 92037, USA.

[4]Mass Spectrometry Core, Beth Israel Deaconess Medical Center, Boston, MA 02215, USA.

[5]Department of Pharmacology, Weill Cornell Medicine, New York, NY 10065, USA.

[6]Department of Pathology and Laboratory Medicine, Weill Cornell Medicine, New York, NY 10065, USA.

[7]Division of Signal Transduction, Beth Israel Deaconess Medical Center and Department of Medicine, Harvard Medical School, Boston, MA 02215, USA.

[8]Dana Farber Cancer Institute, Boston, MA 02215, USA.

[9]Current address: Emory University, Atlanta, GA 30322, USA.

[10]Current address: Amgen, Thousand Oaks, CA 91320, USA.

[*]Co-corresponding authors. **Corresponding Authors:** Benjamin D. Stein Ph.D., Weill Cornell Medicine, 413 E 69th Street, BB750, New York, NY 10021 USA, Phone: 646-962-6333, bds2005@med.cornell.edu; Harold Varmus M.D., Weill Cornell Medicine, 413 E 69th Street, BB1322, New York, NY 10021 USA, Phone: 646-962-7254, varmus@med.cornell.edu; Lewis C. Cantley, Ph.D., Dana Farber Cancer Institute, 450 Brookline Ave, Smith Building, Rm 970, Boston, MA 02215-5450 USA, Phone: 617-632-5034, lewis_cantley@dfci.harvard.edu.

Author Contributions

B.D.S., H.V., and L.C.C. conceived of and designed the study. H.V. and L.C.C. supervised the study. B.D.S. guided and performed most experiments, performed all proteomics and biochemical experiments, metabolomics experiments, computational analyses, and generated the KPCas9 and both KLCas9 mouse models. J.R.F. provided reagents and analyzed clinical data. E.E.G., D.W. and B.N. assisted in xenograft studies. E.E.G. performed some 3D Matrigel experiments, all *in vivo* tail vein and allograft studies. J.W.C., J.S.C. and R.E.M. performed and analyzed chemical trapping metabolomics data. M.Y. and J.M.A. performed metabolomics analyses. Q.C., M.S. and S.S.G. analyzed metabolomics experiments. P.E.H. and R.J.S. provided cell-lines and lysates utilized for A549 proteomics. C.Z. analyzed comparative histological staining. R.J.L. performed seahorse experiments. B.D.S. wrote the manuscript, which was reviewed by all authors.

Conflict of Interest Disclosure: L.C.C. is a co-founder and member of the SAB and holds equity in Faeth Therapeutics, Volastra Therapeutics and Larkspur Therapeutics. He is also a co-founder, former member of the SAB and BOD and holds equity in Agios Pharmaceuticals. H.V. is a member of the SABs of Volastra, Dragonfly Therapeutics, and Surrozen. R.E.M. is a co-founder and consultant for Anastasis Biotec Ltd., and co-founder, Director, and consultant for ReAx Biotechnologies. These companies are developing novel therapies for cancer. L.C.C.'s laboratory has previously received some financial support from Petra Pharmaceuticals. None of these companies are developing drugs related to the research in this paper. All other authors declare no competing interests.

[11]Current address: University of Texas – Southwestern, Dallas, TX 75390, USA.

[12]Current address: Washington University in St. Louis, Saint Louis, MO 63130, USA.

[13]Current address: Memorial Sloan Kettering Cancer Center, New York, NY 10021, USA.

[14]These authors contributed equally

Abstract

KRAS is the most frequently mutated oncogene in human lung adenocarcinomas (hLUAD) and activating mutations frequently co-occur with loss-of-function mutations in *TP53* or *STK11/LKB1*. However, mutation of all three genes is rarely observed in hLUAD, even though engineered co-mutation is highly aggressive in mouse lung adenocarcinoma (mLUAD). Here we provide a mechanistic explanation for this difference by uncovering an evolutionary divergence in regulation of triosephosphate isomerase (TPI1). In hLUAD, TPI1 activity is regulated via phosphorylation at Ser21 by the Salt Inducible Kinases (SIKs) in an LKB1-dependent manner, modulating flux between completion of glycolysis and production of glycerol lipids. In mice, Ser21 of TPI1 is a Cys residue which can be oxidized to alter TPI1 activity without a need for SIKs or LKB1. Our findings suggest this metabolic flexibility is critical in rapidly growing cells with *KRAS* and *TP53* mutations, explaining why loss of LKB1 creates a liability in these tumors.

STATEMENT OF SIGNIFICANCE: Utilizing phospho-proteomics and metabolomics in genetically engineered human cell-lines and GEMMs we uncover an evolutionary divergence in metabolic regulation within a clinically relevant genotype of human LUAD with therapeutic implications. Our data provide a cautionary example of the limits of GEMMs as tools to study human diseases such as cancers.

INTRODUCTION:

Lung cancer remains the most common cause of cancer mortality in the United States and worldwide, due to high incidence coupled with poor response to standard-of-care therapies in most patients.(1) However, lung cancer is not a single disease, but comprises a spectrum of distinct sub-types that arise from different cellular origins, governed by specific somatic mutations affecting different sets of proto-oncogene and tumor suppressor genes.(2-5)

Previous genomic research has defined the underlying genetic mutations that govern specific disease subtypes and have revealed genotypes that are favored or disfavored in the mutational landscape of numerous cancers, including lung adenocarcinoma (LUAD).(6-10) In efforts to understand these combinations of mutations in cancers of the lung and other tissues, most attention has been accorded to the selective advantages of mutations that promote cell growth and other tumorigenic traits referred to as “hallmarks of cancer”.(11,12) But some combinations of mutations, such as mutations that activate both the *EGFR* and *KRAS* oncogenes, are detrimental to cancer cells and selected against.(13,14)

Metabolic reprogramming is a cancer hallmark, required to support tumorigenesis in diverse environments.(15,16) Despite improvements in our understanding of metabolic discrepancies between normal and oncogenic tissues, accurately modeling and exploiting these differences for therapeutic intervention has achieved only marginal success. The

serine/threonine protein kinase, Liver Kinase B1 (LKB1) has been defined as a conserved central regulator of metabolic processes under both physiological and pathological contexts.(17,18) LKB1 governs organismal and cellular response to energy stress by activation of members of a family of kinases, the AMPK-related kinases (AMPKRs), with the role of AMP-activated protein kinase (AMPK) most extensively defined.(19-21) Further research is needed to annotate the role of other AMPKRs in governing metabolic stress response.

Inherent differences between humans and mice may also have significant effects on tumor development, through divergent mechanisms of response to the oxidative environment and to metabolic determinants.(22) The nature and extent of such differences are unknown, but their mechanisms may reveal new molecular targets for therapy.

In this report, we have examined why the three most common genetic mutations found in human LUAD - loss-of-function *TP53* mutations, oncogenic *KRAS* activation, and loss-of-function *LKB1* mutations - rarely co-occur, despite earlier observations that loss of LKB1 is associated with more aggressive growth of LUADs in genetically engineered mouse models harboring *TP53* and *KRAS* mutations.(23-27) Therefore, we sought to identify differences between human and mouse lung adenocarcinoma (hLUAD and mLUAD) with the most common genotype, mutated *KRAS* and *TP53* (KP-mutant), and to determine the effects of loss of the tumor suppressor *LKB1* on metabolic regulation and the growth of such tumors. We have focused on two especially intriguing aspects of the problem: the role of LKB1 in metabolic reprogramming and the physiological consequences conferred by species-specific differences in the sequence of a critical enzyme governing cell metabolism, triose phosphate isomerase (TPI1). Our findings have implications for the design of therapeutic strategies that affect cancer cell metabolism and for the interpretation of results with mouse models of human cancers.

RESULTS:

Co-occurrence of *KRAS*, *TP53* and *LKB1* mutations differentially affects growth of human and mouse LUADs

We used the TCGA PanCancer Atlas to determine the frequency of co-occurrence of mutations in the three most mutated genes in hLUAD - *KRAS*, *TP53* and *LKB1* - and found that only 8 of 511 tumors carried mutations in all three genes (Figure 1A). A Fisher's Exact test showed that the co-occurrence of *LKB1* and *TP53* mutations in hLUADs with a *KRAS* mutation was less frequent than expected by chance, based on the overall frequency of mutations in these three genes, with an odds ratio of 0.35 and a P-value of 0.01 (Figure 1B). No similar reduction was observed in the co-mutation of *TP53* and *LKB1* in the absence of *KRAS* mutations (odds ratio = 0.95; p-value of 0.87) (Figure 1B). A second data set from Memorial Sloan Kettering Cancer Center derived from sequencing of tumor DNA from 1,357 lung cancer patients revealed similar infrequency of triple mutations (Figures S1A and S1B).(9)

While mutations in *KRAS*, *TP53* and *LKB1* together are rare in hLUAD, previous studies have shown that genetically engineered mouse models (GEMMs) harboring conditional mutations in all three genes develop mLUAD that is more aggressive and more likely

to metastasize than with only two of these genes mutated.(23-27) To investigate this discrepancy between LUAD in human patients and mouse models, we generated isogenic human and mouse KP cell lines with and without LKB1 and also compared them to existing GEMM-derived tumor lines with parallel genotypes.(25) Human KP lines engrafted and formed tumors *in vivo*, whereas isogenic lines in which *LKB1* was deleted (KPL) did not (Figure 1C). Furthermore, human KP lines from two different human KP LUAD parental cell-lines readily formed spheroids in organotypic culture, but KPL lines did not or were substantially regressed (Figure S1C and S1D). In contrast, mouse isogenic cell lines both formed tumors *in vivo* with subsequent Lkb1 inactivation accelerating observed tumor growth (Figure 1D), where GEMM-derived KP and KPL lines both formed tumors *in vivo* and spheroids *in vitro* with equal frequency (Figures S1E and S1F). Additionally, treatment of human isogenic lines in organotypic culture with the *KRAS* G12C inhibitor, AMG-510, reduced spheroid formation of a G12C mutant KP line, but partially rescued spheroid growth of a KPL line (Figure S1G).

To determine whether these observations were attributable to LKB1 kinase activity, wildtype or kinase-inactive (K78I) LKB1 were re-expressed in multiple isogenic KPL hLUAD lines. We first verified that wildtype LKB1 restored the activity of AMP-activated protein kinase (AMPK), a known substrate of LKB1, under conditions of energy stress. Glucose restriction caused LKB1-dependent phosphorylation of AMPK at Thr172 and of its downstream substrates (Acetyl CoA Carboxylase (ACC) at Ser79, Raptor at Ser792, and Unc-51 Like autophagy activating Kinase 1 (ULK1) at Ser555) (Figures 1E and S1H). Expression of wildtype (WT), but not kinase-inactive (KI) LKB1, rescued growth of xenografts in immunodeficient mice, suggesting that LKB1 kinase activity is required to support tumor formation by human KP LUAD cells (Figure 1F).

Phosphorylation of human TPI1 is LKB1-dependent

Since LKB1 phosphorylates and activates a family of AMPK-related Ser/Thr protein kinases (AMPKRs) involved in regulating various metabolic and stress response pathways, we used comprehensive quantitative proteomics and phospho-proteomics under glucose-limited conditions to assess differences in protein phosphorylation between KP and KPL isogenic human lines. Phosphorylation of Ser21 on the glycolytic enzyme Triosephosphate Isomerase (TPI1) was one of the most significantly down-regulated phosphorylation events observed when comparing KPL to KP (Figures 2A, S2A and S2B), with peptide identification and phospho-site localization confirmed by manual inspection of the derived MS/MS spectra (Figure S2C). This effect was not due to differences in protein levels as observed in our corresponding total proteomic analyses in multiple human KP and KPL isogenic lines (Figures 2B, S2D and S2E). Furthermore, utilizing a developed phospho-specific antibody against P-Ser21 of TPI1 confirmed phospho-proteomic results and validated this phosphorylation as an LKB1 dependent event (Figure 2C). In contrast, using the same experimental design with tumor-derived mouse cell lines, we did not detect phosphorylation of Tpi1 in cells with either KP or KPL genotypes, although TPI1 protein levels were reduced in cells with a KPL genotype (Figures 2D and 2E).

To assess if restoration of LKB1 kinase activity re-established phosphorylation of TPI1 during metabolic stress, we used quantitative proteomics and phospho-proteomics to analyze human KPL cells expressing WT or KI LKB1 in parallel with KP and KPL cells under glucose-limited conditions. Again, Ser21 was one of the sites at which phosphorylation was most significantly reduced when KPL cells and KPL cells expressing exogenous KI LKB1 were compared with KP cells and KPL cells expressing WT LKB1 (Figure 2F). Quantification of phospho-peptide ion intensities within individual genotypes confirmed restoration of p-Ser21 levels in human KPL lines expressing WT, but not KI LKB1 (Figure 2G), without significant variation in the abundance of TPI1 protein.

Phosphorylation of TPI1 regulates triose phosphate levels and metabolic flux

To examine the possibility that loss of regulation of TPI1 in hLUAD might explain selection against the KPL genotype, we studied the metabolic consequences of LKB1 deficiency. It is known that TPI1 controls interconversion of the triose phosphates, dihydroxyacetone phosphate (DHAP) and glyceraldehyde-3-phosphate (GAP), both of which are generated by aldolase from the upstream glycolytic intermediate fructose-1,6-bisphosphate (F-1,6-BP). This conversion in carbon metabolism lies at a critical bifurcation point: one product, GAP, is used for glycolysis and energy homeostasis, whereas the other, DHAP, is used for lipid synthesis and cellular growth, and it has recently been shown to activate the mammalian Target of Rapamycin protein kinase (mTOR).(28) Additionally, previous studies have shown that increased oxidative burden due to *KRAS* and/or *TP53* mutations cause metabolic flux to flow primarily through the oxidative Pentose Phosphate Pathway (oxPPP) to increase reductive potential and restore redox balance.(29-31)

We assessed the influence of LKB1-dependent phosphorylation on TPI1 activity by measuring the pools of GAP and DHAP in KP and KPL hLUAD cell lines. Due to the inherent instability and complex chromatographic separation of the triose phosphates, we used *in situ* chemical-trapping metabolomics with hydroxylamine labeling of live cells under normal and glucose-limited conditions to create quantifiable, stable adducts (Figures 3A and S3A).(32) These analyses confirmed the relative elevation of DHAP in KPL lines under normal and low glucose, further suggesting that TPI1 phosphorylation limited DHAP accumulation to maintain GAP for glycolysis (Figures 3B and S3B). Additionally, in a parallel analysis of KPL cell lines re-expressing WT and KI LKB1, levels of GAP and DHAP in LKB1 WT lines more accurately replicated endogenous levels in KP human cells, while DHAP remained elevated in LKB1-KI cells (Figure S3C). Furthermore, steady-state analysis revealed that human KPL cells had a significant increase in glycerol-3-phosphate (G3P), the next metabolic intermediate in lipid and triglyceride synthesis, in response to both normal and low glucose (Figures 3C and S3D). Collectively, the observed changes in metabolites and phosphorylation of human TPI1 suggested that LKB1 regulates distribution of glycolytic metabolites via the triose phosphates through a regulatory phosphorylation site of TPI1.

To ascertain the extent to which glucose-derived central carbon flux was affected by loss of LKB1 in human KP LUAD, we conducted Metabolic Flux Analysis (MFA) using positionally-labeled 1,2-$^{13}C_2$ glucose under low (0.5 mM) glucose conditions at 0.5, 1, 2

and 5 minutes. The positional labeling of glucose allowed for accurate assessment of the flux of glucose-derived carbon through primary glycolysis, lipid synthesis, and oxPPP by monitoring differences in isotopic incorporation of key metabolic intermediates in each pathway (Figure 3D). More importantly, this tracer allows annotation of TPI1 activity more broadly within the context of central carbon metabolism, as the three carbons that produce GAP from F-1,6-BP would be unlabeled (M+0), and any observed incorporation of both labeled carbons (M+2) into GAP and lower glycolytic intermediates would require conversion of DHAP to GAP by TPI1. If oxPPP is a route to generate GAP for lower glycolysis and the TCA cycle, single carbon labeled (M+1) intermediates would be observed in significant amounts and can be readily determined by 3-phospoglycerate (3-PG) isotopologue distribution (Figure 3D).(33-35)

We first looked at differential incorporation of both carbons (M+2) into the glycolytic intermediates F-1,6-BP, GAP and 3-PG, as well as the oxPPP intermediate, 6-phosphogluconate (6-PG). We observed reduced incorporation of all glycolytic intermediates and an increase in 6-PG incorporation in the KPL versus KP hLUAD cells, with a linear increase of incorporation across the time course for F-1,6-BP and 6-PG (Figures 3E and S3E). The increase in 6-PG incorporation suggested that oxPPP flux may be higher in KPL. However, neither an appreciable accumulation of singly labeled carbon (M+1) incorporation into GAP and 3-PG, nor a significant difference between KP and KPL hLUAD cells were observed. However, differences in unlabeled (M+0) GAP and 3-PG was observed at later time-points, suggesting a difference in primary glycolytic flux (Figure S3F and S3G). In addition, when we measured fractional incorporation of M+2 into the lipid and triglyceride synthesis pathway intermediate G3P, we observed a significant increase at all time points in KPL when compared to KP hLUAD cells (Figure 3F).

Given the observed difference in metabolic flux after *LKB1* was mutated in human KP LUAD cells, we next assessed mitochondrial function and metabolic rate in mouse and human LUAD lines with different genotypes. Human and mouse LUAD cells grown in normal or low glucose were analyzed for mitochondrial respiration and metabolic rate. Strikingly, maximal respiration was blunted in human KPL compared to KP lines, but no significant differences were found in the GEMM-derived mouse lines with KP and KPL genotypes (Figures 3G and S3H). Additionally, Extracellular Acidification Rate (ECAR) values supported a pronounced defect in metabolic rate selectively in human KPL cells. Under normal (11.1 mM) glucose conditions, ECAR values for human KPL cells were similar to those in KP cells grown under low (0.5 mM) glucose conditions. This discordance was not observed in the mouse counterparts (Figures 3G and S3H). Collectively, the MFA and mitochondrial stress results indicate that the reduced central carbon flux observed in KPL hLUAD is diverted into lipid and triglyceride synthesis pathways, contributing to a metabolic defect, and compromised mitochondrial respiration not observed in mLUAD cells with a KPL genotype.

LKB1-activated members of the Salt Inducible Kinase family phosphorylate human TPI1

We next sought to determine whether human TPI1 is phosphorylated directly by LKB1 or by one of the downstream LKB1-dependent Ser/Thr protein kinases of the AMPKR family;

these kinases, all of which require phosphorylation by LKB1 for activity, are known to mediate responses to various metabolic stresses (Figure 4A).(18,36,37)

To determine whether AMPKR kinases are directly responsible for TPI1 phosphorylation downstream of LKB1, we monitored phosphorylation of Ser21 in TPI1 in a panel of human *KRAS;LKB1*-mutant LUAD cell lines in which sub-families of the AMPKR kinases have been mutated, after restoring stable expression of WT LKB1 from a transgene (Figure 4B).(24) Restoration of LKB1 increased the phosphorylation of Ser21 in TPI1, consistent with results in Figure 2E and 2F, and inactivation of the Salt Inducible Kinase (SIK) subfamily significantly reduced Ser21 phosphorylation (Figure 4B). Mutational inactivation of other AMPKR super-family members [the Microtubule Affinity Regulating Kinases (MARKs), the NUAK Family Kinases (NUAKs), the Brain-Specific Serine/Threonine-Protein Kinases (BRSKs), the catalytic subunits of AMPK, and SNF Related Kinase (SNRK)] did not have significant effects on phosphorylation of TPI1 at Ser21. Furthermore, by analyzing specific combinations of SIK family member mutants, we found that SIK1 and SIK3 together made the greatest contribution to phosphorylation of Ser21 in TPI1 (Figure S4A).

Supporting the concept that the SIK sub-family of protein kinases drive phosphorylation of Ser21 in TPI1, phosphorylation of Ser551 in SIK3, known to regulate activity by altering molecular association, was one of the most significantly down-regulated phosphorylation sites in the LKB1-inactivated, KP-mutant hLUAD cell lines (Figure S2B).(38,39) Additionally, phosphorylation of Ser62, Ser329 and Ser370 in CREB Regulated Transcription Coactivator 3 (CRTC3), all SIK family substrate sites, were also reduced in KPL versus KP human lines (Figures S2A and S2B). Furthermore, we found that the amount of *SIK1* mRNA was significantly increased upon inactivation of *LKB1* in multiple human KP lines, suggesting that a signaling network might increase transcription of *SIK1* via a feedback mechanism to recover SIK activity after loss of LKB1 (Figure S4B).

We next asked if SIK family kinases were responsible for phosphorylation of TPI1 in human KP lines that express LKB1 from the endogenous *LKB1* locus. We generated a series of cell lines deficient in members of the *SIK* gene family, including two *SIK1/2/3* triple knockout lines (SIK TKO). Analysis of this series of cell lines by western blot confirmed deletion of all SIK family members in the SIK TKO lines (Figure S4C). A quantitative total proteomic analysis of KP hLUAD cells under low glucose conditions with various combinations of deletions of *SIK1*, *SIK2* and *SIK3* in KP hLUAD revealed numerous proteomic changes (Figure S4D). However, the amount of TPI1 protein was not significantly altered (Figure S4E). Quantitative phospho-proteomic analyses on the same cells under low glucose revealed that Ser21 in TPI1 was among the phosphorylation events with the greatest reduction when SIK TKO cells were compared with SIK WT cells, mirroring LKB1 loss. In addition, numerous proteins and phospho-sites known to regulate the cell cycle, including CHEK1 and FOSL1 were affected; the latter findings were validated by Western blot analysis without a notable difference in phospho-ERK1/2 (Figures 4C and S4F). Additionally, measurements of the TPI1 p-Ser21 tryptic peptide from these cells indicated that each of the SIK kinases contribute to phosphorylation of TPI1 at Ser21 in KP hLUAD cells downstream of LKB1 (Figure 4D). Furthermore, SIK TKO in KP hLUAD cells phenocopied LKB1 loss in compromised mitochondrial respiration and extracellular

acidification under normal and low glucose conditions and reduced spheroid formation in organotypic culture (Figures 4E and 4F).

These results indicate that in the examined KP hLUAD cell lines, the SIK family of LKB1-regulated protein kinases appear to dominate the phosphorylation of Ser21 in TPI1. However, since deletion of all three SIK family members did not eliminate phosphorylation at this site, other LKB1-regulated protein kinases may also contribute to TPI1 phosphorylation or compensate for loss of the SIK kinases.

Non-conserved amino acid sequence of TPI1 requires LKB1 to regulate its multimeric state in human but not mouse LUAD

To determine whether differences between LKB1 loss in human and mouse LUAD cells could be explained by differences in regulation of TPI1/Tpi1, we explored the evolutionary conservation of the primary amino acid sequence surrounding position 21 of this enzyme. Ser21 and the surrounding residues are conserved in most mammals and other metazoans, including yeast. However, in mouse and rat Tpi1, Ser21 has been replaced by cysteine (Figure 5A). In a published crystal structure of human TPI1, the hydroxyl moiety of Ser21 is located at a region of subunit:subunit interactions, presumably stabilizing the homodimer. Notably, the nearby residues Arg18 and Lys19 form inter-subunit electrostatic interactions predicted to further stabilize the highly active homodimer state. This structure raises the possibility that phosphorylation of Ser21 could produce intra-subunit charge interactions with Arg18 and/or Lys19, interfering with the ability of these amino acids to confer stability to the dimer, thereby altering enzymatic activity (Figure 5B).(40) Since the sulfur atom of Cys21 in rodent Tpi1 could be oxidized to sulfinic or sulfonic acid, mimicking phosphorylation of Ser21, it is possible that rodents have a mechanistic alternative to phospho-dependent regulation of TPI1 activity. This could explain differences in the response to loss of LKB1 in mouse and human KP tumors, circumventing the requirement for LKB1 activity in murine tumors in response to stress.

Based on the structural features of human and mouse TPI1/Tpi1, we asked whether the loss of LKB1 kinase activity and reduced phosphorylation of human TPI1 at Ser21 would differentially affect the dimerization and activity of this enzyme in cells from the two species. We used native gel electrophoresis (BN-PAGE) and Western blot to determine the proportions of monomeric and dimeric TPI1 in extracts of two human KP cell lines, in the presence and absence of LKB1, when cells are grown under normal glucose conditions (Figure S5A). Loss of LKB1 promoted the dimeric (more slowly migrating) form of the human TPI1 protein; conversely, cell lines expressing LKB1 had increased monomeric TPI1 (Figure S5A). Furthermore, analysis of one set of isogenic hLUAD lines under normal and low glucose conditions revealed that LKB1 loss dictated the biophysical distribution of dimeric and monomeric TPI1 under both growth conditions and that the availability of environmental glucose had no observable effects (Figure 5C). Thermal Proteome Profiling (TPP) was also used to measure the thermal stability of TPI1 proteoforms.(41,42) The ΔTm (measured at 0.5 fraction non-denatured) of the phosphorylated variant was 5.8°C lower than that of unmodified TPI1, further supporting the prediction that phosphorylation of Ser21 limits dimerization of TPI1 (Figure 5D).

In contrast, we observed no changes in the ratio of the monomeric and dimeric forms of mouse Tpi1 in KP versus KPL cell lines grown in media with normal or low glucose concentrations (Figure 5E). However, acute treatment of mouse lines with the oxidant peroxide caused a dramatic shift towards the monomeric form of Tpi1 in low glucose medium, independent of Lkb1 status (Figure 5E). Additionally, peroxide treatment caused a similar shift towards monomeric Tpi1 under normal (11.1 mM) glucose conditions in KPL, but not in KP mouse cells (Figure 5E), consistent with earlier reports that loss of Lkb1 increases basal oxidative stress.(43-46)

To further explore the functional significance of the amino acid difference at position 21 of TPI1 and Tpi1 and its effect on homodimer formation, we created a series of tagged TPI1 variants expressed as transgenes in human KP cells following CRISPR/Cas9-mediated depletion of endogenous *TPI1*. Replacement of Serine with Alanine (S21A) increased recovery of both the transgenic and remaining endogenous TPI1 by immunoprecipitation under competitive, antibody-limited conditions and low glucose treatment, implying that an inability to phosphorylate position 21 of TPI1 stabilized the TPI1 dimer. In contrast, the phospho-mimetic S21D mutant form of TPI1 or a mutant in which Ser21 is replaced by an oxidizable cysteine (S21C) significantly reduced co-immunoprecipitation of the remaining endogenous TPI1 under low or normal glucose conditions, with no observed effect from acute oxidant treatment with diamide in the latter (Figure 5F and S5B). These findings were further confirmed when TPI1 variants were analyzed by BN-PAGE. Wildtype transgenic human TPI1 was found in both the dimeric and monomeric states, but the S21A mutant was detected solely in the dimeric state, and the S21C variant was mostly monomeric (Figure S5C). Collectively, these findings support the conclusion that phosphorylation of human TPI1 or oxidation of murine Tpi1 destabilizes its dimeric form, providing a structural mechanism by which TPI1/Tpi1 activity can be regulated in response to LKB1-dependent phosphorylation or by oxidative stress.

To gauge the phenotypic effects of single amino acid substitutions at position 21 of TPI1 we created an untagged allelic panel of TPI1 variants following CRISPR/Cas9-mediated depletion of endogenous TPI1 and verified loss of phosphorylation (Figure 6A). First, we tested TPI1 allelic variants in both human KP and KPL isogenic lines for spheroid growth in organotypic culture (Figure 6B). As seen previously, all TPI1 variants in the KPL isogenic cells were substantially reduced in spheroid growth, in both size and number, relative to TPI1 allelic variants in isogenic KP cells. Strikingly, we also observed near complete ablation of observable spheroid formation of the S21A variant in the KPL cells, further suggesting that regulation of this site is critical upon LKB1 loss in KP hLUAD (Figure 6B). To verify our previous Metabolic Flux Analyses, we next conducted isotopic tracing in our human TPI1 allelic variants in both KP and KPL isogenic cells using positionally-labeled 1,2-$^{13}C_2$ glucose under low (0.5 mM) glucose conditions at 1 minute. When we measured fractional incorporation of M+2 into the lipid and triglyceride synthesis pathway intermediate G3P, we again observed a statistically significant increase in all TPI1 variants in the KPL genotype when compared to KP hLUAD cells, except for TPI1 S21D which was compelling (Figure 6C). Additionally, we observed a similar effect when we looked at differential incorporation of both carbons (M+2) into GAP, where again only TPI1 S21D in the KPL cells showed a reduction in incorporation when compared to TPI1 S21D expressing

KP cells, with no significant difference observed for any other TPI1 variant in KP versus KPL genotypes (Figure S6A). Furthermore, no change was observed when comparing TPI1 variants in KP versus KPL cells for the glycolytic intermediates F-1,6-BP and 3-PG (Figures S6B and S6C), as well as the oxPPP intermediate, 6-PG (Figure S6D). Lastly, we engrafted all TPI1 variant cell-lines into the flanks of athymic nude mice to look for changes in tumor growth rates. We observed the most pronounced reduction in tumor growth with the TPI1 S21D variant expressed in human KPL cells (Figure 6D).

These unexpected observations with the TPI1 S21D variant suggested the possibility of an unusual mechanistic event., During the revision of our manuscript, a study reported the use of native mass-spectrometry and *in vitro* reconstitution experiments to deduce that TPI1 Ser 21 phosphorylation existed in a hemi-phosphorylated state in the TPI1 dimer (i.e. only 1 of 2 monomers is phosphorylated).(47) Furthermore, this phosphorylation increased enzymatic activity by four-fold over the unmodified dimer. The authors found no evidence of a doubly phosphorylated TPI1 dimer in both cell-lysate or from *in vitro* re-constitution studies, which collectively supports our biochemical, metabolomic, and allelic xenograft data, suggesting that TPI1 S21D would be the most deleterious allele for tumor growth because TPI1 would be entirely monomeric.

To assess the effects of TPI1 alterations on tumor growth and explore the therapeutic relevance of TPI1 as a target, we generated conditional KPCas9 and two different KLCas9 (v1 and v2) mouse models that can inactivate genes targeted by CRISPR-mediated mutagenesis (*KRAS G12D*$^{LSL/+}$;*Trp53*$^{fl/fl}$;*R26*$^{LSL/LSL}$*Cas9-IRES-GFP*, *KRAS G12D*$^{LSL/+}$;*Lkb1*$^{fl/fl}$;*R26*$^{LSL/LSL}$*Cas9-IRES-GFP* and *KRAS G12D*$^{LSL/+}$;*Lkb1*$^{fl/fl}$;*H11*$^{LSL/LSL}$*Cas9*;*R26*$^{LSL/LSL}$*tdTomato*; see Methods) (Figure 7A). Tumor-derived mLUAD cell lines were established from these mice and used to characterize the functional consequences of genetic changes by injection into immune-competent, syngeneic hosts. CRISPR/Cas9-mediated mutation of *Lkb1* in KPCas9 tumor cells (now KPLCas9 cells) delivered by tail vein injection reduced median survival of mice by approximately 50% compared to control cells, with increased lung colonization and tumor burden (Figure 7B and S7A). Conversely, mutational inactivation of *Tpi1* permitted 100% survival of mice receiving tail vein injections, with blunted lung colonization and absence of clearly defined tumor lesions in the experimental time sampled (Figure 7B and S7A). We next compared Tpi1 loss by paired flank injections in syngeneic hosts of isogenic KP vs. KPL cells and observed that loss of Tpi1 in both KP and KPL significantly reduced tumor volume one month following engraftment (Figure 7C).

We next assessed the effects on tumor growth and lung colonization of single amino acid variations at position 21 in mouse Tpi1 in our tumor-derived cell-lines. As with our human TPI1 allelic panels, CRISPR-based mutation of endogenous Tpi1 was followed by expression of transgenes encoding sgRNA-resistant WT, C21A, C21D, C21E or C21S versions of Tpi1 and we tested for evidence of phosphorylation using the previously derived phospho-specific antibody. Results verified that the C21S variant is phosphorylated in the mouse tumor derived KPcas9 cells (Figure S7B). Furthermore, deletion of Lkb1 in culture or *de novo* generation of tumor derived KPLCas9 cells by administration of sgTrp53 gRNA with Cre-recombinase in our KLCas9v1 model and generation of additional Tpi1 allelic

variants revealed reduced phosphorylation of Tpi1 C21S by both routes (Figure S7C). Next, tail vein injection of the established KPCas9 Tpi1 allelic panel was conducted to assess lung colonization and tumor burden in response to a single amino acid substitution. No difference was observed in tumor lesions per lobe or lesion diameter between re-expression WT and C21A, however both C21D and C21S resulted in significant reduction in both tumor burden and tumor size in the lung (Figure 7D and 7E). Additionally, histological staining revealed reduced colonization of the lung, and absence of clearly defined tumor lesions using cells with Tpi1 C21D and C21S, with the same time course previously for cells in which Tpi1 had been mutationally inactivated (Figure 7B and S7A), phenocopying those observations (Figure S7D).

Given these collective observations, we next explored the effects on tumor growth of single amino acid variations at position 21 in mouse Tpi1 in our derived Cysteine to Alanine or Serine in mouse Tpi1 isogenic KP and KPL cells by injection into the flanks of syngeneic hosts. Paired engraftment into mice demonstrated that transgenic re-expression of Tpi1 WT showed increased tumor volume in KPL vs. KP as previously observed (Figure 7F). However, KPL cells with C21A Tpi1 produced smaller tumors, whereas little or no effect on tumor size was observed when C21A Tpi1 was produced in KP cells, further supporting the necessity of regulating Tpi1 at position 21 upon *Lkb1* loss and confirming our lung colonization data (Figures 7B, 7D and 7E). KP and KPL tumor cells producing C21S Tpi1 both showed reduced tumor volumes, and previous Western blot analysis (Figure S7C) suggests that residual phosphorylation is still present in the Lkb1-inactivated lines.

Lastly, we asked if inactivation of Tpi1 in an autochthonous lung cancer model was disadvantageous. Utilizing our KLCas9v2 GEMM we intratracheally administered equivalent titers of lentiviral particles encoding Cre-recombinase and guide RNAs targeting *Tpi1* (sgTpi1) or a non-targeting control (sgNT). Median survival of mice receiving LentiCre/sgNT (KLN) was 52 days, in line with previous reports on the latency of KL lung tumorigenesis.(24,48-51) However, mice administered LentiCre/sgTpi1 (KLT) had a median survival of 96 days (Figure 7G). Comparative histology when KLN mice exhibited labored breathing (2 months) revealed tumor burden that was multifocal/multinodular in both KLN and KLT mice, but KLN mice had larger, more diffuse tumors. In contrast, lesions in KLT mice were smaller and less diffuse (Figure 7G). KLT mice had normal appearing lung tissue in between the tumor nodules, while in KLN mice there was diffuse spreading of tumor cells along the alveolar septa (i.e. lepidic growth) (Figure S8A). Additionally, histology in moribund KLT mice on study greater than 90 days revealed sustained, well-demarcated lesions with no observable lepidic growth, suggesting distinct pathology and tumor progression upon Tpi1 inactivation (Figure 7G and S8A). Finally, to confirm whether observed lesions fully inactivated Tpi1, we performed immunofluorescence on temporally-matched, tumor-bearing lungs. While Tpi1 is expressed in all cells, and highly expressed in infiltrating immune/proliferative cells, the smaller lesions from KLT mice were less intense in their staining for Tpi1 (Figure S8B). However, all KLT mice died from lung tumor burden, and examination of these late lesions showed an increase in Tpi1 signal as compared to early stage tumors (Figure S8B). Therefore, we cannot rule out that Tpi1 was inactivated in every tumor cell, and a significant amount of tumor mass observed may be attributed to tumor cells that escaped Tpi1 inactivation. Taken together, these results suggest that TPI1

may be a relevant therapeutic target in KP hLUAD and validate the identified regulatory axis as a contributing factor in the selection against the KPL genotype in human LUAD.

DISCUSSION:

Although much progress has been made using GEMMs to decipher mechanisms of tumor initiation and progression, comparisons of human and mouse tumors often lead to conflicting observations.(52) In particular, accurately recapitulating the tumor metabolic environment remains a significant challenge, but an important one, since discrepancies between mouse and human tumors are likely to have implications in development of novel therapeutic agents.(53) Here we provide a mechanistic explanation for why the loss of LKB1 in hLUADs driven by *KRAS* and *TP53* mutations is a rare event that appears to be selected against in human tumors, but not in mouse tumors, where the loss of *Lkb1* enhances tumorigenesis and metastasis.

Several recent reports have implicated the SIK kinases as effectors of LKB1-mediated tumor suppression in *Kras*- and *Kras*;*Tp53*-mutant mLUAD; however, similar findings have not been reported in hLUADs.(24,27) Here we find that this discrepancy may be due, in part, to a single amino acid difference between rodent and other metazoan versions of the glycolytic enzyme TPI1. In turn, that difference can influence subsequent metabolic events, which determine the flow of glucose-derived tri-carbon substrates into pathways for glycolysis or lipid synthesis. In humans, the abundance of the products of TPI1 is governed by the LKB1-SIK-TPI1 signaling axis that we have elucidated in this manuscript. In rodents, the substitution of an oxidizable cysteine for a phosphorylatable serine at residue 21 of Tpi1 enables direct redox regulation, circumventing the requirement for regulation by LKB1-SIK-mediated phosphorylation.

Our biochemical, proteomic, and metabolomic data support the conclusion that phosphorylation of TPI1 in hLUAD regulates the biophysical distribution of monomeric and dimeric forms, altering enzymatic activity and in turn triose phosphate pools. This reduces the conversion of GAP to DHAP, an energetically downhill reaction, and thereby shifts the balance away from glycerol lipid production and towards alternate metabolic pathways, including glycolysis and the TCA cycle. Regulation of metabolites at this central point in the glycolytic pathway could help to overcome metabolic stresses experienced during tumorigenesis and to improve the efficiency of energy production. In addition, this regulation allows rapidly growing cells to balance pathways for lipid synthesis versus serine/glycine synthesis. Collectively, these metabolic differences could strongly influence a wide range of pro-tumorigenic processes and have significant effects on tumor cell phenotype, all of which warrant future study.

Additional features of these phenomena - such as how specific *KRAS* and *TP53* mutations influence this phenotype and their contributions to the response to metabolic and oxidative stresses - have yet to be deciphered. Previous research suggests that *TP53* can upregulate the enzyme TIGAR in response to oxidative and metabolic stresses, which suggests a critical role for p53 expression in response to LKB1 loss with anticipated increased oxidative stress.(30,54-56) Yet further work is needed to decipher whether TIGAR expression is

differentially affected in p53 null versus p53 mutant cells. In fact, our preliminary data suggests that homozygous deleted *TP53* KP hLUAD cells (NCI-H358) respond more poorly to acute LKB1 loss than *TP53* mutant KP hLUAD cells (NCI-H2009) in organotypic culture and warrants further investigation (Figure S1C and S1D).

Knowledge of the differences in human and mouse TPI1/Tpi1 may explain not only the different consequences of loss of LKB1 in human and mouse LUADs; it may also help to design next-generation mouse models in which the mechanisms of metabolic regulation of human cancers are more accurately replicated. Furthermore, the findings reported here suggest that selective inhibitors of LKB1 or of SIK family protein kinases could be effective in treating human *KRAS/TP53* mutant lung cancers or other cancers with *KRAS/TP53* mutations. Our work also raises the cautionary note that preclinical trials with such inhibitors would likely fail in currently available GEMMs with *Kras* and *Tp53* mutations.

Finally, the observations reported here also reveal new ways for LKB1 to regulate metabolism, beyond its known capacity to respond to cellular energy levels through activation of AMPK.(20) While enzymes such as hexokinase, pyruvate kinase, and phosphofructokinase have been intensely studied in regard to phosphorylation-dependent regulation in cancers, TPI1 has not been considered a likely factor in cancer-dependent regulation of metabolic flux. Additional research is needed to understand whether regulation of TPI1 by LKB1 is important in other types of human cancers and whether this knowledge provides a basis for seeking new cancer therapies across multiple organ types and mutational backgrounds.

Methods

No statistical methods were used to predetermine sample size. Data were visualized and statistical analyses performed using Prism 9 software (Graph Pad) or R statistical package. $P < 0.05$ was considered statistically significant. P values for paired comparisons between two groups with comparable variance were calculated by two-tailed Student's t-test.

Reagents

Media and sera were purchased from Life Technologies and R&D Systems respectively. AMG-510 (sotorasib) was acquired from Selleck Chemicals (Catalog No. S8830). All other reagents were from Sigma-Aldrich unless otherwise noted.

Cell lines

All cell lines (A549, H358, H441, H2009, 634T and HEK293T) were purchased from ATCC or kindly provided by Kwok-Kin Wong at NYU Langone Medical Center (634T and Lkb1-t2). Cells were maintained in RPMI 1640 medium (Life Technologies: 11879020) supplemented with glucose concentrations as indicated (Life Technologies: A2494001) except for HEK293T cells, which were propagated in DMEM with sodium pyruvate and L-glutamine (Corning). All media supplemented with 10% FBS, 100 units/ml of penicillin and 100 μg/ml streptomycin and grown at 37°C in a 5% CO_2, humidified incubator. All cell lines were confirmed to be mycoplasma-free using the MycoAlert mycoplasma detection kit (Lonza: LT07-218).

CRISPR/Cas9 reagents, plasmids

The control and LKB1-KO lines were generated by infecting the cell lines with lentivirus generated from the LentiCRISPRv2 plasmid (Addgene: 52961). The control and TPI1-KO or SIK-KO lines were generated by infecting the Cas9-expressing lines (LentiCRISPRv2) with lentivirus generated from the LRT2B plasmid (Addgene: 110854). The sgRNA sequences are as follows: sgNT1, CCAATACGGACCGGATTGCT; sgLKB1-2, TGTATAACACATCCACCAGC; sgLKB1-3, TGCACAAGGACATCAAGCCG; sgSAFE, GGTTGGATAAGGCTTAGAAA; sgTPI1-3, GAAGTACACGAGAAGCTCCG; sgTPI1-4, GGAAGCCATCCACATCAGGC; sgSIK1, ATGGTCGTGACAGTACTCCA; sgSIK2, GCACCGGATCACCAAGACGG; sgSIK3, GTGCTTGCAGATCTGCTCCA; sgTpi1, TGAAGGTCAGTACAAACGCA. The TPI1 alleles were synthesized by Twist Biosciences and cloned into pHAGE-CMV-N-Flag-HA-IRES-Puro-DEST or pLenti-PGK-Hygro via Gateway cloning or Gibson Assembly using NEB HiFi DNA Assembly Master Mix.

Lentivirus production, transduction and single-cell cloning

Lentivirus was generated by transfecting the target plasmid with the packaging plasmids pMD2.G (Addgene: 12259) and psPAX2 (Addgene: 12260) into 293T cells using Lipofectamine 3000 (Invitrogen: L3000015). Media was changed 6 hours after transfection, and then the viral supernatant was collected at 24 and 48h post-transfection. Transduction was conducted in 6 well format on 1 x 10^5 cells and cells plated in suspension into viral supernatant containing 8 μg/ml Polybrene (Santa Cruz Biotechnology: SC-134220) and incubated overnight (16h). Viral supernatant was aspirated, and fresh culturing media added to transduced cells for recovery for 24h. Puromycin (Life Technologies: A1113803) was supplemented into media 48h post-transduction for relevant plasmids (LentiCRISPRv2 and pHAGE-CMV-N-Flag-HA-IRES-PURO) at a concentration of 2 μg/ml and selection conducted for 72h. Blasticidin (Invivogen: ANT-BL-1) was supplemented into media 48h post-transduction for relevant plasmid (LRT2B) at a concentration of 10 μg/ml and selection conducted for 5 days. Following selection, single cell cloning was conducted by serial dilution and plating into a 96 well plate, and cells were maintained under relevant selection criteria during the cloning process. Clones that grew out from single cells were expanded and validation of knockout conducted by Western-blot or qPCR as indicated.

LUAD clinical data set analysis

Human LUAD (hLUAD) datasets (TCGA and MSKCC) were downloaded from cBioPortal and KRAS, TP53, and LKB1 mutational and copy number status were assessed. Samples were divided into KRAS-mutant and KRAS-wild-type cohorts for further analysis. Using the R statistical software package, a Fisher's exact test was performed on each cohort to determine the odds of TP53 and LKB1 mutations co-occurring.

Athymic nude mice and xenografts

Animal procedures were performed with the approval of the Weill Cornell Medicine IACUC. Tumor volume was not allowed to exceed 1000 mm^3 in any experiment. Prior to implantation, cells were re-suspended in PBS and mixed 1:1 with Matrigel (Corning,

356231). Cells were then injected subcutaneously into single flanks of 6-week-old male and female athymic mice (Envigo). Caliper measurements were performed weekly to monitor tumor growth. For the H358 LKB1-KO clones, 1 x 10^6 cells were injected per flank; for the murine lung tumor lines (634T and Lkb1-t2) 1 x 10^4 cells were injected per flank.

Western blotting

Protein lysates were prepared in CST lysis buffer (Cell Signaling Technology: 9803) supplemented with cOmplete mini EDTA free protease inhibitor (Roche: 04693159001) and quantified using the BCA protein assay (Thermo Scientific, 23225). Lysates prepared at a concentration of 1 mg/ml and supplemented with 4x Laemmli Sample Buffer (Bio-Rad: 1610747) supplemented with fresh 2-mercaptoethanol (Sigma: M3148). Proteins were separated on self-cast Tris-glycine polyacrylamide gels, transferred to Polyscreen PVDF membranes (Perkin Elmer: NEF1002), and probed with Cell Signaling Technology antibodies used at 1:1000 in 5% BSA (Sigma: A4503) in TBS-T: P-ACC Ser79 (#3661), ACC (#3662), P-Raptor Ser792 (#2083), Raptor (#2280), P-AMPKα Thr172 (#2535), AMPK α1/2 (#2532), LKB1 (#3047), P-ULK1 Ser555 (#5869), ULK1 (#8054), SIK2 (#6919), P-FRA1(FOSL1) Ser265 (#5841) and Phospho-p44/42 MAPK (Erk1/2) Thr202/Tyr204 (#4370). Antibodies from Abcam used at concentrations indicated in 5% BSA in TBS-T against β-actin (ab6276, 1:20,000), TPI1 (ab96696, 1:3,000) and P-SIK1 Thr182 + P-SIK2 Thr175 + P-SIK3 Thr163 (ab199474, 1:1000). Antibody from Novus Biologicals was used at 1:20,000 in 5% BSA in TBS-T against SIK3 (NBP2-47278). Antibodies from Sigma-Aldrich against Flag epitope tag (F7425, 1:5,000) and (F3165, 1:1000) were used at indicated concentrations in 5% BSA in TBS-T. Secondary antibodies from Millipore against Rabbit (AP132PMI) and Mouse (AP124PMI) primary antibodies were resuspended per manufacturer's instructions and used at 1:10,000 in 5% non-fat dried milk in TBS-T. Western blots were then developed in the dark room on an autoradiograph following incubation with home-made ECL.

Immunoprecipitation

Following indicated treatments, cells were rinsed in ice cold PBS collected and lysed in ice-cold CST lysis buffer (Cell Signaling Technology: 9803) supplemented with cOmplete mini EDTA free protease inhibitor (Roche: 04693159001) and rotated end-over-end for 30 minutes at 4°C. The soluble fraction of each lysate was generated by centrifugation at 13,200 RPM for 15 minutes at 4°C and supernatant transferred to clean microcentrifuge tubes. Generated lysates were then pre-cleared with Protein A Dynabeads (Invitrogen: 10001D) pre-equilibrated in CST lysis buffer for 1 hour with gentle rocking at 4°C. Pre-cleared lysates were then centrifuged at 500 x g, placed on a magnet for 2 minutes and supernatant moved to clean microcentrifuge tubes. Clarified soluble protein lysate was then quantified by micro BCA assay (Thermo Scientific, 23225). Following quantification, 1 milligram of each lysate was then incubated with 1.2 μg of TPI1 polyclonal antibody (Proteintech # 10713-1-AP) for 16 hours at 4°C. Following 16 hour incubation, samples were supplemented with 10ul pre-equilibrated protein A Dynabeads and allowed to incubate at 4°C for the additional hour rotating end-over-end. Immunoprecipitated proteins bound to the resin were then washed 3 times in cold lysis buffer, and proteins were eluted from beads by pulse boiling in Laemmli sample buffer (Bio-Rad) for 5 minutes at 90°C. Following

boiling the mixture was centrifuged at 500 x g at room temperature for 5 minutes, then placed on a magnet for 2 minutes to separate beads and the supernatants loaded onto gel for Western blot analysis.

Sn-glycerol-3-phosphate steady state analysis metabolite extraction

Cells were cultured in medium reconstituted from glucose-free RPMI 1640 medium (Life Technologies: 11879020) supplemented with 11.1 or 0.5 mM glucose and 10% dialyzed FBS. The day prior to treatment and collection cells were lifted and counted and 2 x 10^6 cells were plated in a 10cm culture dish. Cells were rinsed twice with PBS before the addition of normal or low glucose medium. Metabolites were extracted at 30 minutes post addition as indicated in text.

Metabolic Flux Analysis

Cells were cultured in medium reconstituted from glucose-free RPMI 1640 medium (Life Technologies: 11879020) supplemented with 0.5 mM 1,2 $^{13}C_2$ glucose (Cambridge Isotope Laboratories: CLM-504-PK) and 10% dialyzed FBS. The day prior to treatment and collection cells were lifted and counted and 2 x 10^6 cells were plated in a 10cm culture dish in RPMI 1640 medium supplemented with 11.1 mM glucose and 10% FBS. Cells were given a medium change 1 h before the addition of tracing medium and glucose conditions were lowered to 0.5 mM Glucose at this time. Cells were rinsed twice with PBS before the addition of tracing medium. The time of addition of tracer medium was designated time 0. Metabolites were extracted at 0.5, 1, 2, and 5 minutes post addition as indicated in text N=6 per genotype and time-point and PBS washes were not implemented at the collection time-point to ensure accurate collection times.

Metabolite extraction and liquid chromatography– tandem mass spectrometry (LC–MS/MS) analysis

Cells were washed twice with PBS, and twice with LC-MS grade H_2O (except for tracing analyses). Five hundred μl of 80% methanol at −80 °C was added to quench metabolic reactions and the cells were collected by scraping. The lysate was then transferred to a fresh 2.0 ml Eppendorf tube pre-chilled on dry-ice and an additional 500 μl of 80% methanol was added to the original plate and scraped again. The second lysate was added to the first and incubated on dry ice for 20 minutes with intermittent vortexing then centrifuged at 16,000g for 10 min to allow cellular debris to be pelleted. The aqueous volume was then transferred to a clean, fresh pre-chilled 2.0 ml Eppendorf tube and dried under vacuum in a speedvac and stored at −80°C. Dried sample pellets were resuspended in HPLC-grade water (20 μl) and centrifuged at 20,000 g for 5 min to remove insoluble material. Following centrifugation, 16 μl of supernatant was transferred to virgin polypropylene auto sampler vials, capped and placed on dry ice. Supernatants (5 μl) were injected and analyzed using a hybrid 6500 QTRAP triple quadrupole mass spectrometer (AB/SCIEX) coupled to a Prominence UFLC HPLC system (Shimadzu) via selected reaction monitoring (MRM). ESI voltage was +4950V in positive ion mode and –4900V in negative ion mode with polarity switching. A dwell time of 3 ms per SRM transition was used. Approximately 10–12 data points were acquired per detected metabolite. Q1/Q3 SRM transitions were developed to target both the unlabeled and labeled isotopomer forms of each tested metabolite in either

positive or negative mode. Samples were delivered to the mass spectrometer via hydrophilic interaction chromatography (HILIC) using a 4.6 mm i.d. x 10 cm Amide XBridge column (Waters) at 400 μl/min using a chilled autosampler. Gradients were run starting from 85% buffer B (HPLC grade acetonitrile) to 42% B from 0 to 5 min; 42% B to 0% B from 5 to 16 min; 0% B was held from 16 to 24 min; 0% B to 85% B from 24 to 25 min; 85% B was held for 7 min to re-equilibrate the column. Buffer A was comprised of 20 mM ammonium hydroxide/20 mM ammonium acetate (pH = 9.0) in 95:5 water:acetonitrile. Peak areas from the total ion current for each metabolite SRM transition were integrated using MultiQuant v3.0 software (AB/SCIEX). Tubes containing cellular debris was retained to determine protein concentration for data normalization. Briefly pellet was resuspended by addition of 600 μl of sodium hydroxide and boiled at 90 °C for 30 minutes with intermittent vortexing. Resolubilized pellets were allowed to come to room temperature, and protein quantified using the DC protein assay (Bio-Rad: 5000111). Derived metabolite data was normalized to protein concentration and median ion intensity per injection across the dataset.

In situ hydroxylamine trapping in live cells

Two 15 cm dishes per condition were plated with 9 x 10^6 cells 24 hr prior to treatment. Plated cells were washed twice with PBS then grown in RPMI 1640 media containing 11.1 mM or 0.5 mM glucose as indicated for 6 hr. Cells were then washed twice with PBS and 3 ml of PBS containing protease inhibitors was added to the plate and cells were scraped. Cell homogenate was transferred to a 15ml conical tube and centrifuged at 1,400 x g for 3 minutes to pellet cells. Cellular pellets were resuspended in 300 μl ice cold 80% Methanol and transferred to a 1.5 ml Eppendorf tube. Chemical labeling of live cells was achieved by adding 10 μl of hydroxylamine solution (Sigma: 467804, ~15M solution) and incubated for 10 minutes with gently vortexing intermittently. Following a 10 minute incubation, the suspended cells were lysed with a probe sonicator set to 30% amperage pulse (1:1 pulse:pause 16 seconds total). Lysed cellular homogenates were then centrifuged at 20,000 x g for 10 minutes at 4 °C. Clarified supernatant was transferred to a fresh 1.5 ml Eppendorf tube and dried under Nitrogen gas flow until all solvent was evaporated. Dried pellets were then stored at −80 °C until ready for analysis. Dried metabolites were resuspended in 100 μL of an 80:20 mixture of MeOH/H_2O and an internal deuterated standard, 10 nmol d_3-serine, was added to the dried metabolome solution for quantification and sample normalization.

Targeted LC-MS/MS for hydroxylamine trapping

Resuspended metabolites were separated by hydrophilic interaction chromatography with a Gemini reverse-phase C18 column (50 mm x 4.6 mm with 5 μm diameter particles) from Phenomenex together with precolumn (C18, 3.5 mm, 2 mm X 20 mm). Mobile phase A was composed of 100% H_2O (10 mM tributylamine aqueous solution, adjusted to pH 4.95 with 15 mM acetic acid), and mobile phase B was composed of 100% Methanol. Using a multi-step gradient with buffer A and B: 0-5 min, 95% A; 5-15 min, 95-90% A; 15-22 min, 90-85% A; 22-26 min, 10% A, and maintained for 4 min; 30-33 min, 95% A, and maintained for 7 min. The flow rate was 0.2 ml/min for 0-15 min and 30-40 min, and 0.3 ml/min for 15-30 min. Targeted MS/MS analysis was performed on an Agilent triple quadrupole LC-MS/MS instrument (Agilent Technologies 6460 QQQ). The capillary voltage was set to 4.0 kV. The drying gas temperature was 350°C, the drying gas flow rate was 10

L/min, and the nebulizer pressure was 45 psi. Relative metabolite abundance was quantified by integrated peak area for the given MRM-transition. Data presented are representative of three independent biological experiments each containing three technical replicates for a given condition.

Proteomics and phospho-proteomic sample preparation

Protein lysates were prepared in CST lysis buffer (Cell Signaling Technology: 9803) supplemented with cOmplete mini EDTA free protease inhibitor (Roche: 04693159001) and quantified using the BCA protein assay (Thermo Scientific, 23225). Following quantification, 100 μg of each protein lysate was moved into a clean 1.5 mL tube. Following distribution of protein, each tube was brought to a final volume of 300 μL by addition of PBS, followed by precipitation with trichloroacetic acid (TCA) (Sigma) to a final concentration of 25%, vigorously vortexed and incubated on ice overnight. TCA precipitates were centrifuged at 21,130 *x g* for 30 minutes at 4°C, washed twice in 500 μL of ice-cold acetone, and centrifuged at 21,130 *x g* for 10 minutes after each wash. Following precipitation and washes, pellets were allowed to completely dry at room temperature. Dry pellets were re-suspended in 100 μL of 100 mM TEAB, 0.5% SDS and reduced with 9.5 mM tris-carboxyethyl phosphine (TCEP) for 60 minutes at 55°C. Following reduction of disulfide bonds with TCEP, the denatured protein mix was centrifuged at 21,130 *x g* for 5 minutes then alkylated with 4.5 mM iodoacetamide (IA) for 30 minutes in the dark at room temperature. After reduction and alkylation of disulfide bonds, the denatured protein mixture was precipitated out of solution by addition of 600 μL of ice-cold acetone and placed in the −20°C freezer overnight. The following day precipitated proteins were centrifuged at 8,000 *x g* for 10 minutes to pellet precipitated protein. Following centrifugation supernatant was decanted off and pellets were allowed to air-dry at room temperature. Once dry, protein pellets were reconstituted in 100 μL 100 mM TEAB and $CaCl_2$ was supplemented to a final concentration of 1 mM, 2 μg of sequencing grade Trypsin (Promega) was added, and reactions were placed in the dark on a thermal mixer (Eppendorf) set to 37°C and shaking at 850 r.p.m. for 16 hours.

Thermal Proteomic Profiling

Cells were lifted using TrypLE Express (Thermo Fisher Scientific - GIBCO) and neutralized following 5-minute incubation using complete media (RPMI + 10% FBS penicillin/streptomycin) and centrifuged at 1100 r.p.m. for 4 minutes. The cell pellet was reconstituted in 10 mL PBS containing protease and phosphatase inhibitors (Roche) and centrifuged again at 1100 RPM for 4 minutes. Following centrifugation, the cell pellet was resuspended in 1 mL PBS with inhibitors and distributed into thin-wall PCR tubes at 100 μL of cell suspension in each tube. Thermal denaturation was performed as previously described, and the resulting cellular suspension was transferred to clean 1.5 mL microcentrifuge tubes and PCR tubes were additionally rinsed with 30 μL of PBS with inhibitors to ensure complete transfer of cellular suspension. Cellular suspension was next snap frozen in liquid nitrogen for 1 minute followed by thawing and re-equilibration back to room temperature. This freeze-thaw cycle was repeated 2 additional times and the soluble fraction of each lysate was generated by centrifugation at 21,130 *x g* for 30 minutes at 4°C. Supernatants were transferred to clean 1.5 mL microcentrifuge tubes, and protein was quantified in

the supernatant for temperatures 37°C and 41°C by micro-BCA assay (Thermo Fisher Scientific - Pierce). Following quantification, the average of the two lowest temperatures was taken and the volume equivalent to 30 μg of protein in the lowest temperature was moved from each temperature fraction into a clean 1.5 mL tube. Following distribution of protein, each tube was brought to a final volume of 300 μL by addition of PBS with inhibitors, followed by precipitation with trichloroacetic acid (TCA) (Sigma) to a final concentration of 25%, vigorously vortexed and incubated on ice overnight. TCA precipitates were centrifuged at 21,130 *x g* for 30 minutes at 4°C, washed twice in 500 μL of ice-cold acetone, and centrifuged at 21,130 *x g* for 10 minutes after each wash. Following precipitation and washes, pellets were allowed to completely dry at room temperature. Dry pellets were re-suspended in 100 μL of 100 mM TEAB, 0.5% SDS and reduced with 9.5 mM tris-carboxyethyl phosphine (TCEP) for 60 minutes at 55°C. Following reduction of disulfide bonds with TCEP, the denatured protein mix was centrifuged at 21,130 *x g* for 5 minutes then alkylated with 4.5 mM iodoacetamide (IA) for 30 minutes in the dark at room temperature. After reduction and alkylation of disulfide bonds, the denatured protein mixture was precipitated out of solution by addition of 600 μL of ice-cold acetone and placed in the −20°C freezer overnight. The following day precipitated proteins were centrifuged at 8,000 *x g* for 10 minutes to pellet precipitated protein. Following centrifugation supernatant was decanted off and pellets were allowed to air-dry at room temperature. Once dry, protein pellets were reconstituted in 100 μL 100 mM TEAB and $CaCl_2$ was supplemented to a final concentration of 1 mM, 1 μg of sequencing grade Trypsin (Promega) was added, and reactions were placed in the dark on a thermal mixer (Eppendorf) set to 37°C and shaking at 850 r.p.m. for 16 hours. The next day, digested samples were centrifuged at 21,130 *x g* for 10 minutes and proceeded to TMT labeling of digested samples.

TMT labeling, fractionation, and phosphopeptide enrichment

TMT labeling was performed generally as per manufacturer's protocol. Briefly, each TMT tag was re-suspended in 164 μL anhydrous acetonitrile with intermittent vortexing for 10 minutes. Following resuspension, 41 μL was added to corresponding temperatures (TMT-126 = 37°C; four separate aliquots of each temperature for subsequent desalting and fractionation) and labeling reaction was allowed to proceed for 1 hour at room temperature. Reactions were quenched by addition of 8 μL of 5% hydroxylamine in 100 mM TEAB and incubated for 15 minutes. Labeled temperature fractions were pooled, desalted on 1cc/50 mg C18 SepPAK columns (Waters # WAT054955) on a vacuum manifold and desalted peptides were dried down in a speedvac. Dried peptides were reconstituted in 300 μL of 0.1% TFA in H_2O, high-pH reverse phase spin-columns (Thermo fisher scientific - Pierce) were equilibrated, and samples fractionated per manufacturer's instructions into 8 fractions, 2 washes and a flow-through fraction (11 total). Separate samples from the same fractions were then combined and dried. Peptide fractions were reconstituted in 200 μL of 5% acetonitrile, 0.1% TFA in water, and 10 μL was removed for bulk HTP analysis. The remaining fractionated labeled peptides dried and re-dissolved in 40% acetonitrile, 6% TFA in water before phosphopeptide enrichment with Titansphere 5 μm TiO_2 beads (GL Sciences). Titansphere TiO2 beads (GL Sciences) were reconstituted in buffer containing 80% acetonitrile, 6% TFA, and 2,5-dihydroxybenzoic acid (20 mg/mL) and rotated for 15 min at 25°C. Equal amount of beads slurry (~5:1 beads-to-peptide ratio based on

concentration of peptides in 37°C aliquot) was added to each temperature aliquot of reconstituted peptides and rotated for 20 mins 25°C. Beads were then washed twice with higher percentage of acetonitrile (10% and 40%) in 6% TFA and supernatant was removed by centrifugation at 500 *x g* for 2 min. Washed beads were then added to self-packed stage tip with C8 SPE (Sigma Aldrich) and washed once more with 60% acetonitrile in 6% TFA. Phosphopeptides were first eluted with 5% NH_4OH, then 10% NH_4OH, 25% acetonitrile, and dried with speedvac. Dried phosphopeptides were reconstituted in 5% acetonitrile, 1% TFA, desalted with self-packed stage tip with C18 SPE (Sigma Aldrich), and dried with speedvac once more. The final processed phosphopeptides were reconstituted in 5% acetonitrile, 0.1% TFA in water for LC-MS^3 analysis.

LC-MS^3 analysis and data acquisition

High-pH reverse-phase fractions were run on a 4-hour instrument method with an effective linear gradient of 180 minutes from 5% to 25% mobile phase B with the following mobile phases: A: 0.1% formic acid in H_2O, B: 80% acetonitrile/0.1% formic acid in water on a 50 cm Acclaim PepMap RSLC C18 column (Thermo Fisher Scientific #164942) operated by a Dionex ultimate 3000 RSLC nano pump with column heating at 50°C connected to an Orbitrap Fusion Lumos. Briefly, the instrument method was a data-dependent analysis and cycle time set to 3 seconds, total. Each cycle consisted of one full-scan mass spectrum (400-1500 m/z) at a resolution of 120,000, RF Lens: 60%, maximum injection time of 100 ms followed by data-dependent MS/MS spectra with precursor selection determined by the following parameters: AGC Target of $4.0e^5$, maximum injection time of 100 ms, monoisotopic peak determination: peptide, charge state inclusion: 2-7, dynamic exclusion 10 sec with an intensity threshold filter: $5.0e^3$. Data-dependent MS/MS spectra were generated by isolating in the quadrupole with an isolation window of 0.4 *m*/z with CID activation and corresponding collision energy of 35%, CID activation time of 10 ms, activation Q of 0.25, detector type Ion Trap in Turbo mode, AGC target of 1.0e4 and maximum injection time of 120 ms. Data-dependent multi-notch MS^3 was done in synchronous precursor selection mode (SPS, multi-notch MS^3) with the following settings: Precursor selection Range; Mass Range 400-1200, Precursor Ion Exclusion Properties *m*/z Low: 18 High: 5, Isobaric Tag Loss Exclusion Properties: TMT. Number of SPS precursors was set to 10 and data-dependent MS^3 was detected in the Orbitrap (60,000 resolution, scan range 120-500) with an isolation window of 2 *m*/z HCD activation type with collision energy of 55%, AGC target of 1.2e5 and a maximum injection time of 150 ms. Raw files were parsed into MS1, MS2 and MS3 spectra using RawConverter.

Proteomic, phospho-proteomic and thermal profiling data analysis

Data generated were searched using the ProLuCID algorithm in the Integrated Proteomics Pipeline (IP2) software platform. Human and Mouse proteome data were searched using concatenated target/decoy UniProt databases. Basic searches were performed with the following search parameters: HCD fragmentation method; monoisotopic precursor ions; high resolution mode (3 isotopic peaks); precursor mass range 600-6,000 and initial fragment tolerance at 600 p.p.m.; enzyme cleavage specificity at C-terminal lysine and arginine residues with 3 missed cleavage sites permitted; static modification of +57.02146 on cysteine (carboxyamidomethylation), +229.1629 on N-terminal and lysine for TMT-10-

plex tag; 4 total differential modification sites per peptide, including oxidized methionine (+15.9949), and phosphorylation (+79.9663) on serine, threonine, and tyrosine (only for phospho-enriched samples); primary scoring type by XCorr and secondary by Zscore; minimum peptide length of six residues with a candidate peptide threshold of 500. A minimum of one peptide per protein and half-tryptic peptide specificity were required. Starting statistics were performed with a Δmass cutoff = 10 p.p.m. with modstat, and trypstat settings. False-discovery rates of protein (pfp) were set to 1% (for unenriched datasets) or peptide (sfp) set to 1% (for phospho-proteomics datasets). TMT quantification was performed using the isobaric labeling 10-plex labeling algorithm, with a mass tolerance of 5.0 p.p.m. or less. Reporter ions 126.127726, 127.124761, 127.131081, 128.128116, 128.134436, 129.131417, 129.13779, 130.134825, 130.141145, and 131.13838 were used for relative quantification.

Seahorse analysis

OCR and ECAR measurements were performed using a Seahorse XFe96 analyzer (Seahorse Biosciences). Seahorse XFe96 plates were coated with 0.56ug Cell-Tak (Corning) in 24 mL coating buffer (8 mL H2O + 16 mL. In vitro cultured cells were collected and plated in 96 well plated at 40,000 cells per well 16 hours prior to analysis in Seahorse RPMI media PH7.4 (Agilent, 103576-100) supplemented with 11.1 mM Glucose (Agilent) and 10% FBS. To measure the OCR and ECAR of normal and low glucose treated cells, Seahorse RPMI media PH 7.4 was supplemented with 11.1 mM or 0.5 mM glucose (agilent) and previously plated cells were washed 2x with PBS then media added as indicated with 6 representative wells per cell-line and glucose concentration. Respiratory rates were measured in RPMI Seahorse media, pH7.4 (Agilent) supplemented with 11.1 or 0.5 mM glucose (Agilent) and 2mM glutamine (Agilent) in response to sequential injections of oligomycin (1 mM), FCCP (0.5 mM) and antimycin/rotenone (1 mM) (all Agilent: 103015-100). Following analysis media was aspirated from analyzed cells and 50 ul of RIPA lysis buffer was directly added and micro-bca (pierce) conducted to normalized results to protein concentration.

KRAS G12D$^{LSL/+}$;*TP53*$^{fl/fl}$;*R26* $^{LSL/LSL}$*Cas9-IRES GFP* (KPCas9) mouse model

All transgenic animals were bred and maintained in the animal facility of Weill Cornell Medicine with the approval of the university IACUC panel (protocol #: 2013-0116). *KRAS G12D*$^{LSL/+}$ mice were obtained from Jackson Laboratory (JAX; B6.129S4-*Kras*^{tm4Tyj}/J; Strain #:008179) and maintained on a C57BL/6J background (JAX; C57BL/6J; Strain #:000664). *TP53*$^{fl/fl}$ mice were obtained from Jackson Laboratory (JAX; B6.129P2-*Trp53*^{tm1Brn}/J; Strain #:008462). *R26* $^{LSL/LSL}$*Cas9-IRES GFP* mice (JAX; B6J.129(B6N)-*Gt(ROSA)26Sor*$^{tm1(CAG-cas9*,-EGFP)Fezh}$/J; Strain #: 026175). *TP53*$^{fl/fl}$ mice were crossed to *R26* $^{LSL/LSL}$*Cas9-IRES GFP* mice then heterozygous progeny were backcrossed. Homozygous mice were then backcrossed for 3 generations to generate *TP53*$^{fl/fl}$*; R26* $^{LSL/LSL}$*Cas9-IRES GFP* mice. Concurrently *KRAS G12D*$^{LSL/+}$ mice were crossed to *R26* $^{LSL/LSL}$*Cas9-IRES GFP* mice. Confirmed progeny were then crossed to *R26* $^{LSL/LSL}$*Cas9-IRES GFP* mice. Confirmed progeny were then backcrossed for 3 generations to *R26* $^{LSL/LSL}$*Cas9-IRES GFP* mice. Next F3 generation *TP53*$^{fl/fl}$*; R26* $^{LSL/LSL}$*Cas9-IRES GFP* mice were crossed and back crossed to F3 *KRAS G12D*$^{LSL/+}$; *R26* $^{LSL/LSL}$*Cas9-IRES GFP* mice to generate *KRAS G12D*$^{LSL/+}$; *TP53*$^{fl/fl}$*; R26* $^{LSL/LSL}$*Cas9-IRES GFP* progeny.

Confirmed mice were maintained by continual breeding to previously generated F3 *TP53$^{fl/fl}$; R26 $^{LSL/LSL}$Cas9-IRES GFP* mice for 4 generations prior to use.

KRAS G12D$^{LSL/+}$;LKB1$^{fl/fl}$;R26 $^{LSL/LSL}$Cas9-IRES GFP (KLCas9v1) mouse model

All transgenic animals were bred and maintained in the animal facility of Weill Cornell Medicine with the approval of the university IACUC panel (protocol #: 2013-0116). *KRAS G12D$^{LSL/+}$* mice were obtained from Jackson Laboratory (JAX; B6.129S4-*Kras^{tm4Tyj}*/J; Strain #:008179) and maintained on a C57BL/6J background (JAX; C57BL/6J; Strain #:000664). *LKB1$^{fl/fl}$* mice were obtained from Jackson Laboratory (JAX; STOCK *Stk11$^{tm1.1Sjm}$*/J; Strain #:014143). *R26 $^{LSL/LSL}$Cas9-IRES GFP* mice (JAX; B6J.129(B6N)-*Gt(ROSA)26Sor$^{tm1(CAG-cas9*,-EGFP)Fezh}$*/J; Strain #: 026175). *LKB1$^{fl/fl}$* mice were crossed to *R26 $^{LSL/LSL}$Cas9-IRES GFP* mice then heterozygous progeny were backcrossed. Homozygous mice were then backcrossed for 3 generations to generate *LKB1$^{fl/fl}$; R26 $^{LSL/LSL}$Cas9-IRES GFP* mice. Concurrently *KRAS G12D$^{LSL/+}$* mice were crossed to *R26 $^{LSL/LSL}$Cas9-IRES GFP* mice. Confirmed progeny were then crossed to *R26 $^{LSL/LSL}$Cas9-IRES GFP* mice. Confirmed progeny were then backcrossed for 3 generations to *R26 $^{LSL/LSL}$Cas9-IRES GFP* mice. Next F3 generation *LKB1$^{fl/fl}$; R26 $^{LSL/LSL}$Cas9-IRES GFP* mice were crossed and back crossed to F3 *KRAS G12D$^{LSL/+}$*; *R26 $^{LSL/LSL}$Cas9-IRES GFP* mice to generate *KRAS G12D$^{LSL/+}$*; *LKB1$^{fl/fl}$; R26 $^{LSL/LSL}$Cas9-IRES GFP* progeny. Confirmed mice were maintained by continual breeding to previously generated F3 *LKB1$^{fl/fl}$; R26 $^{LSL/LSL}$Cas9-IRES GFP* mice for 4 generations prior to use.

KRAS G12D$^{LSL/+}$;LKB1$^{fl/fl}$;H11 $^{LSL/LSL}$Cas9;R26 $^{LSL/LSL}$tdTomato (KLCas9v2) mouse model

All transgenic animals were bred and maintained in the animal facility of Weill Cornell Medicine with the approval of the university IACUC panel (protocol #: 2013-0116). *KRAS G12D$^{LSL/+}$* mice were obtained from Jackson Laboratory (JAX; B6.129S4-*Kras^{tm4Tyj}*/J; Strain #:008179) and maintained on a C57BL/6J background (JAX; C57BL/6J; Strain #:000664). *LKB1$^{fl/fl}$* mice were obtained from Jackson Laboratory (JAX; STOCK *Stk11$^{tm1.1Sjm}$*/J; Strain #:014143). *H11 $^{LSL/LSL}$Cas9* mice were obtained from Jackson Laboratory (JAX; B6.129-*Igs2$^{tm1(CAG-cas9*)Mmw}$*/J; Strain #: 027632). *R26 $^{LSL/LSL}$tdTomato* mice were obtained from Jackson Laboratory (JAX; B6.Cg-*Gt(ROSA)26Sor$^{tm14(CAG-tdTomato)Hze}$*/J; Strain #: 007914). *R26$^{LSL/LSL}$tdTomato* mice were crossed to *H11 $^{LSL/LSL}$Cas9* mice then heterozygous progeny were backcrossed. Homozygous mice were then backcrossed for 3 generations to generate *H11$^{LSL/LSL}$Cas9;R26 $^{LSL/LSL}$tdTomato* mice. Next, *LKB1$^{fl/fl}$* mice were crossed and backcrossed to derived *H11$^{LSL/LSL}$Cas9;R26 $^{LSL/LSL}$tdTomato* mice. Concurrently *KRAS G12D$^{LSL/+}$* mice were crossed to *H11$^{LSL/LSL}$Cas9;R26 $^{LSL/LSL}$tdTomato* mice. Confirmed progeny were then backcrossed for 3 generations to *H11$^{LSL/LSL}$Cas9;R26 $^{LSL/LSL}$tdTomato* mice. Next F3 generation *LKB1$^{fl/fl}$;H11 $^{LSL/LSL}$Cas9; R26 $^{LSL/LSL}$tdTomato* mice were crossed and back crossed to F3 *KRAS G12D$^{LSL/+}$*; *H11 $^{LSL/LSL}$Cas9; R26 $^{LSL/LSL}$tdTomato* mice to generate *KRAS G12D$^{LSL/+}$*; *LKB1$^{fl/fl}$; H11 $^{LSL/LSL}$Cas9 R26 $^{LSL/LSL}$tdTomato* progeny. Confirmed mice were maintained by continual breeding to previously generated F3 *LKB1$^{fl/fl}$;H11 $^{LSL/LSL}$Cas9; R26 $^{LSL/LSL}$tdTomato* mice for 4 generations prior to use.

Intratracheal infection

Mice were anesthetized using inhaled 2.5% isoflurane and infected with 10^7 pfu Ad5.Spc-Cre (Iowa Viral Vector Core Facility) via an intranasal or intratracheal route. Infections were performed in a total volume of 50 μL where adenoviral concentrates were gently mixed with serum free EMEM and $CaCl_2$ and allowed to salt out at room temperature for 20' before placing on ice and using within the hour.(57) To knockout specific genes in the mouse airway on top of a tumorigenic genetic background ("KPCas9") guide RNAs were cloned into the Lenti-sgNT/Cre plasmid (gift of M. Winslow; Addgene 66895) using PCR mutagenesis. Crude lentiviral supernatants were generated in HEK-293Ts cells, packaging with psPAX2 (gift of D. Trono; Addgene 12260) and pseudo typed with pMD2.G (gift of D. Trono; Addgene 12259), as above. Following transfection, media was changed at 6hrs and 72hrs supernatants were collected and concentrated using ultracentrifugation above a 30% sucrose cushion for 2 hours at 25,000 rpm (Beckman; SW32 Ti). Supernatants were then discarded, and pelleted lentiviruses were re-suspended overnight at 4C in 200 μL of PBS. Lentiviral titers were determined on early passage tail tip fibroblasts generated from R26R-tdTomato mice (JAX 007908). A titer of ~10^6 virions per mouse was used for indicated experiments and prepared similar to adenoviral concentrates, as detailed above.

Tail tip fibroblast generation

Briefly, mice were euthanized with inhaled carbon dioxide, and the entire tail was excised and sliced lengthwise. The outer epidermis was sheathed and then the remaining tail was sectioned into 1 cm segments and washed 3X with PBS containing Primocin® (Invivogen). Tail sections were placed into culture on plates coated with 0.1% gelatin (Stem Cell Technologies) in DMEM/F12 (Corning) with 10% FBS and 100 μg/mL penicillin/streptomycin (Corning). Three days following fibroblast migration out of tail sections, tail tips were removed, and culture media was replaced every 3-4 days. Primary tail tip fibroblasts were expanded for 2-3 passages before use in lentiviral titer determination.

Lung digestion and generation of lung tumor cell lines

When mice showed labored breathing from advanced disease, animals were euthanized as before, lungs perfused with PBS and inflated through the trachea using 2-3 mL of a mixture containing collagenase type IV (Worthington; LS004188), elastase (Worthington; LS002292), Liberase™ TM (Sigma; 05401119001) and DNAse I (Worthington; LS002139) in serum free EMEM supplemented with 0.5% BSA. Enzyme stock solutions were prepared at 100X working concentrations in water or PBS and stored at −80C prior to use. A hemostat was used to clamp off the trachea, ensuring the digestion cocktail was retaining in the lung and then lobes were grossly dissected away from the heart, thymus and trachea and transferred into a Miltenyi C tube. Using a gentleMACS™ Octo Dissociator, lungs were digested for 45' on a pre-set program. Crude single cell suspensions were then poured over a 70 μm mesh filter (Corning) and washed 3X using PBS containing 0.5% BSA and 1mM EDTA. Red blood cells were lysed for 3' using 5 mL of hypotonic ACK buffer (Gibco) and then cells were washed 2 more times before re-suspension in wash buffer containing DAPI and DNAse I. Viable, EGFP+ or tdTomato+ single cells were sorted on a BD Influx, BD Aria II or Sony MA900 at the Weill Cornell Flow Cytometry Core Facility. Approximately

10^5 sorted cells were plated per well of a 6 well dish in MTEC+ media,(58) and media was changed every 3-4 days until cultures were expanding and required splitting. Once cells lines had adapted to 2D growth in MTEC+ media, they were easily cultured in RPMI-1640 + 10% FBS for further studies. Tumor line genotypes were confirmed by PCR and/or Western blot.

Tail vein in syngeneic hosts

C57Bl/6J mice were purchased from Jackson Laboratories and bred for no more than 4 generations. Both male and female mice, 8-12 weeks of age, were used for these studies. Briefly, mice were anesthetized using inhaled 2.5% isoflurane and vasodilated for 3 minutes with a heat lamp. 5 x 10^5 tumor cells were injected into the right lateral tail vein in a total volume of 100uL of PBS. Following recovery, mice were monitored bi-weekly for 3 months. Survival events were recorded when finding animals dead or moribund from respiratory distress (e.g., gasping).

Allograft in syngeneic hosts

For allograft studies, fur of C57Bl/6J mice was trimmed and then a depilatory cream was applied to both flanks to denude the skin, permitting accurate monitoring of tumor growth. 10^6 tumor cells were subcutaneously injected in a total volume of 100 μL in a 1:1 mixture of PBS and growth factor reduced Matrigel® (Corning). Both male and female mice were used, and in most cases, both hind flanks of mice were used for engraftments. Mice were monitored bi-weekly; tumor volumes were monitored by caliper measurements and calculated using a modified ellipsoid formula. Tumor volumes exceeding $1cm^3$ were outside of protocol limits and when reached, required termination of experiments.

Histology and Tissue Immunofluorescence

Mice were euthanized by carbon dioxide, dissected and lungs were perfused with warm PBS through the left ventricle of the heart. Low melt agarose (2% in PBS) was instilled through the trachea, clamped and then lungs were quickly excised and plunged into freshly prepared, cold 4% paraformaldehyde. Following overnight fixation at 4C, lungs were washed for 30’ in PBS at room temperature and then transferred into 70% ethanol for at least 24hrs. Lobes of lungs were grossly dissected and arranged for embedding to maximize sampled surface areas. Allograft tumor lesions were treated in a similar fashion, omitting cardiac perfusion. Embedding, cutting (4-5uM sections) and routine histologic staining (hematoxylin and eosin) were contracted through Histowiz. Tissue sections were de-waxed in Histoclear® then rehydrated using decreasing alcohol washes and unmasked in a basic retrieval buffer (1X TBS + 0.05% Tween-20 + 2mM EDTA, pH 9.0) for 10’ in a pressure cooker. Slides were cooled in a water bath for 10’ then blocked using 0.5% BSA + 1X TBS + 0.01% Triton X-100 supplemented with mouse-on-mouse blocking reagent (Vector Biolabs MKB-2213-1) for 1 hour at room temperature. Primary antibody incubations were performed overnight at 4C in a humidified chamber (1:500 rabbit anti-RFP; Rockland #600-401-379 or 1:500 rabbit anti-Tpi1; Proteintech® 10713-1-AP). Slides were then washed extensively using TBS + 0.5% Tween-20 and secondary antibody staining was performed at room temperature in the dark for 1 hour (1:1000 DAPI counterstain + 1:1000 donkey anti-rabbit IgG (H+L) Alexa Fluor Plus 594; Thermo Fisher A32754). Slides were again washed extensively, mounted (ProLong® Diamond antifade; Thermo Fisher P36961) and allowed to cure overnight before

imaging. Slides were scanned on an Axio Scan 7 (ZEISS) and images were qualitatively analyzed in Zen 3.5 software. H&E comparisons were reviewed by a pathologist at WCM.

Supplementary Material

Refer to Web version on PubMed Central for supplementary material.

Acknowledgements

We thank Kwok-Kin Wong for kindly providing GEMM derived LUAD cell-lines; 634T and Lkb1-t2. We thank Jianxin Xie and Cell Signaling Technology for generating and kindly providing the Phospho-Ser21 TPI1 antibodies for this study. This work was supported, in part, by NIH grants; P01CA120964 (to L.C.C., R.J.S. and J.M.A.), R35CA197588 (to L.C.C.), R35-CA220538 (to R.J.S.), R01-DK080425 (to R.J.S.), R01AR076029 (to Q.C.) and R21ES032347 (to Q.C.); NSF-CAREER CHE-1945442 (to R.E.M.) and the Alfred P. Sloan Foundation FG-2020-12839 (to R.E.M.). H.V. is the Lewis Thomas University Professor at Cornell University. J.R.F. is the Lee Cooperman Physician-Scientist of the Damon Runyon Cancer Research Foundation (DRG 18-18). E.E.G. is the Kenneth G. and Elaine A. Langone Fellow of the Damon Runyon Cancer Research Foundation (DRG-2343-18). B.N. is supported by a National Cancer Institute (NCI) of the National Institutes of Health (NIH) F99/K00 Career Transition Fellowship (F99CA234950).

Data Availability

All derived UHPLC-MS^3 proteomic data corresponding to data presented in the main figures has been deposited to the ProteomeXchange Consortium through MassIVE (https://massive.ucsd.edu) with the following identifiers:

1. Phospho-proteomic data in Figure 2A: PXD039619 and MSV000091122.
2. Total proteomic data in Figure 2B: PXD039623 and MSV000091125.
3. Phospho-proteomic data in Figure 2D: PXD039639 and MSV000091133.
4. Total proteomic data in Figure 2E: PXD039638 and MSV000091131.
5. Phospho-proteomic data in Figure 2F and 2G: PXD039640, PXD039641 and MSV000091135, MSV000091136.
6. Phospho-proteomic data in Figure 4C and 4D: PXD039650, PXD039659, PXD039677, PXD039678 and MSV000091138, MSV000091140, MSV000091151, MSV000091152

Due to size limitations additional proteomic data corresponding to supplementary figures are available upon request (bds2005@med.cornell.edu).

References:

1. Siegel RL, Miller KD, Jemal A. Cancer statistics, 2020. CA Cancer J Clin 2020;70(1):7–30 doi 10.3322/caac.21590. [PubMed: 31912902]
2. Skoulidis F, Heymach JV. Co-occurring genomic alterations in non-small-cell lung cancer biology and therapy. Nature Reviews Cancer 2019;19(9):495–509 doi 10.1038/s41568-019-0179-8. [PubMed: 31406302]
3. Rudin CM, Poirier JT, Byers LA, Dive C, Dowlati A, George J, et al. Molecular subtypes of small cell lung cancer: a synthesis of human and mouse model data. Nature Reviews Cancer 2019;19(5):289–97 doi 10.1038/s41568-019-0133-9. [PubMed: 30926931]

4. Herbst RS, Heymach JV, Lippman SM. Lung Cancer. New England Journal of Medicine 2008;359(13):1367–80 doi 10.1056/NEJMra0802714. [PubMed: 18815398]
5. Ding L, Getz G, Wheeler DA, Mardis ER, McLellan MD, Cibulskis K, et al. Somatic mutations affect key pathways in lung adenocarcinoma. Nature 2008;455(7216):1069–75 doi 10.1038/nature07423. [PubMed: 18948947]
6. Chang K, Creighton CJ, Davis C, Donehower L, Drummond J, Wheeler D, et al. The Cancer Genome Atlas Pan-Cancer analysis project. Nature Genetics 2013;45(10):1113–20 doi 10.1038/ng.2764. [PubMed: 24071849]
7. Kandoth C, McLellan MD, Vandin F, Ye K, Niu B, Lu C, et al. Mutational landscape and significance across 12 major cancer types. Nature 2013;502(7471):333–9 doi 10.1038/nature12634. [PubMed: 24132290]
8. Campbell PJ, Getz G, Korbel JO, Stuart JM, Jennings JL, Stein LD, et al. Pan-cancer analysis of whole genomes. Nature 2020;578(7793):82–93 doi 10.1038/s41586-020-1969-6. [PubMed: 32025007]
9. Zehir A, Benayed R, Shah RH, Syed A, Middha S, Kim HR, et al. Mutational landscape of metastatic cancer revealed from prospective clinical sequencing of 10,000 patients. Nat Med 2017;23(6):703–13 doi 10.1038/nm.4333. [PubMed: 28481359]
10. Collisson EA, Campbell JD, Brooks AN, Berger AH, Lee W, Chmielecki J, et al. Comprehensive molecular profiling of lung adenocarcinoma. Nature 2014;511(7511):543–50 doi 10.1038/nature13385. [PubMed: 25079552]
11. Hanahan D, Weinberg RA. The Hallmarks of Cancer. Cell 2000;100(1):57–70 doi 10.1016/S0092-8674(00)81683-9. [PubMed: 10647931]
12. Hanahan D, Weinberg Robert A. Hallmarks of Cancer: The Next Generation. Cell 2011;144(5):646–74 doi 10.1016/j.cell.2011.02.013. [PubMed: 21376230]
13. Unni AM, Harbourne B, Oh MH, Wild S, Ferrarone JR, Lockwood WW, et al. Hyperactivation of ERK by multiple mechanisms is toxic to RTK-RAS mutation-driven lung adenocarcinoma cells. eLife 2018;7:e33718 doi 10.7554/eLife.33718. [PubMed: 30475204]
14. Unni AM, Lockwood WW, Zejnullahu K, Lee-Lin S-Q, Varmus H. Evidence that synthetic lethality underlies the mutual exclusivity of oncogenic KRAS and EGFR mutations in lung adenocarcinoma. eLife 2015;4:e06907 doi 10.7554/eLife.06907. [PubMed: 26047463]
15. Pavlova NN, Thompson CB. The Emerging Hallmarks of Cancer Metabolism. Cell Metab 2016;23(1):27–47 doi 10.1016/j.cmet.2015.12.006. [PubMed: 26771115]
16. Chen PH, Cai L, Huffman K, Yang C, Kim J, Faubert B, et al. Metabolic Diversity in Human Non-Small Cell Lung Cancer Cells. Mol Cell 2019;76(5):838–51 e5 doi 10.1016/j.molcel.2019.08.028. [PubMed: 31564558]
17. Alessi DR, Sakamoto K, Bayascas JR. LKB1-Dependent Signaling Pathways. Annual Review of Biochemistry 2006;75(1):137–63 doi 10.1146/annurev.biochem.75.103004.142702.
18. Shackelford DB, Shaw RJ. The LKB1–AMPK pathway: metabolism and growth control in tumour suppression. Nature Reviews Cancer 2009;9(8):563–75 doi 10.1038/nrc2676.
19. Stein BD, Calzolari D, Hellberg K, Hu YS, He L, Hung C-M, et al. Quantitative *In Vivo* Proteomics of Metformin Response in Liver Reveals AMPK-Dependent and -Independent Signaling Networks. Cell Reports 2019;29(10):3331–48.e7 doi 10.1016/j.celrep.2019.10.117. [PubMed: 31801093]
20. Garcia D, Shaw RJ. AMPK: Mechanisms of Cellular Energy Sensing and Restoration of Metabolic Balance. Molecular Cell 2017;66(6):789–800 doi 10.1016/j.molcel.2017.05.032. [PubMed: 28622524]
21. Herzig S, Shaw RJ. AMPK: guardian of metabolism and mitochondrial homeostasis. Nature Reviews Molecular Cell Biology 2018;19(2):121–35 doi 10.1038/nrm.2017.95. [PubMed: 28974774]
22. Demetrius L Of mice and men. When it comes to studying ageing and the means to slow it down, mice are not just small humans. EMBO Rep 2005;6 Spec No:S39–44 doi 10.1038/sj.embor.7400422. [PubMed: 15995660]
23. Eichner LJ, Brun SN, Herzig S, Young NP, Curtis SD, Shackelford DB, et al. Genetic Analysis Reveals AMPK Is Required to Support Tumor Growth in Murine Kras-Dependent Lung

Cancer Models. Cell Metab 2019;29(2):285–302 e7 doi 10.1016/j.cmet.2018.10.005. [PubMed: 30415923]

24. Hollstein PE, Eichner LJ, Brun SN, Kamireddy A, Svensson RU, Vera LI, et al. The AMPK-Related Kinases SIK1 and SIK3 Mediate Key Tumor-Suppressive Effects of LKB1 in NSCLC. Cancer Discov 2019;9(11):1606–27 doi 10.1158/2159-8290.CD-18-1261. [PubMed: 31350328]
25. Liu Y, Marks K, Cowley GS, Carretero J, Liu Q, Nieland TJ, et al. Metabolic and functional genomic studies identify deoxythymidylate kinase as a target in LKB1-mutant lung cancer. Cancer Discov 2013;3(8):870–9 doi 10.1158/2159-8290.CD-13-0015. [PubMed: 23715154]
26. Rogers ZN, McFarland CD, Winters IP, Seoane JA, Brady JJ, Yoon S, et al. Mapping the in vivo fitness landscape of lung adenocarcinoma tumor suppression in mice. Nature Genetics 2018;50(4):483–6 doi 10.1038/s41588-018-0083-2. [PubMed: 29610476]
27. Murray CW, Brady JJ, Tsai MK, Li C, Winters IP, Tang R, et al. An LKB1-SIK Axis Suppresses Lung Tumor Growth and Controls Differentiation. Cancer Discov 2019;9(11):1590–605 doi 10.1158/2159-8290.CD-18-1237. [PubMed: 31350327]
28. Orozco JM, Krawczyk PA, Scaria SM, Cangelosi AL, Chan SH, Kunchok T, et al. Dihydroxyacetone phosphate signals glucose availability to mTORC1. Nature Metabolism 2020;2(9):893–901 doi 10.1038/s42255-020-0250-5.
29. Anastasiou D, Poulogiannis G, Asara JM, Boxer MB, Jiang J-k, Shen M, et al. Inhibition of Pyruvate Kinase M2 by Reactive Oxygen Species Contributes to Cellular Antioxidant Responses. Science 2011;334(6060):1278–83 doi 10.1126/science.1211485. [PubMed: 22052977]
30. Cheung EC, DeNicola GM, Nixon C, Blyth K, Labuschagne CF, Tuveson DA, et al. Dynamic ROS Control by TIGAR Regulates the Initiation and Progression of Pancreatic Cancer. Cancer Cell 2020;37(2):168–82.e4 doi 10.1016/j.ccell.2019.12.012. [PubMed: 31983610]
31. DeNicola GM, Karreth FA, Humpton TJ, Gopinathan A, Wei C, Frese K, et al. Oncogene-induced Nrf2 transcription promotes ROS detoxification and tumorigenesis. Nature 2011;475(7354):106–9 doi 10.1038/nature10189. [PubMed: 21734707]
32. Chang JW, Lee G, Coukos JS, Moellering RE. Profiling Reactive Metabolites via Chemical Trapping and Targeted Mass Spectrometry. Analytical Chemistry 2016;88(13):6658–61 doi 10.1021/acs.analchem.6b02009. [PubMed: 27314642]
33. Antoniewicz MR. A guide to (13)C metabolic flux analysis for the cancer biologist. Exp Mol Med 2018;50(4):19 doi 10.1038/s12276-018-0060-y. [PubMed: 29657327]
34. Jang C, Chen L, Rabinowitz JD. Metabolomics and Isotope Tracing. Cell 2018;173(4):822–37 doi 10.1016/j.cell.2018.03.055. [PubMed: 29727671]
35. Metallo CM, Walther JL, Stephanopoulos G. Evaluation of 13C isotopic tracers for metabolic flux analysis in mammalian cells. J Biotechnol 2009;144(3):167–74 doi 10.1016/j.jbiotec.2009.07.010. [PubMed: 19622376]
36. Sun Z, Jiang Q, Li J, Guo J. The potent roles of salt-inducible kinases (SIKs) in metabolic homeostasis and tumorigenesis. Signal Transduction and Targeted Therapy 2020;5(1):150 doi 10.1038/s41392-020-00265-w. [PubMed: 32788639]
37. Sakamoto K, Bultot L, Göransson O. The Salt-Inducible Kinases: Emerging Metabolic Regulators. Trends in Endocrinology & Metabolism 2018;29(12):827–40 doi 10.1016/j.tem.2018.09.007. [PubMed: 30385008]
38. Berggreen C, Henriksson E, Jones HA, Morrice N, Göransson O. cAMP-elevation mediated by β-adrenergic stimulation inhibits salt-inducible kinase (SIK) 3 activity in adipocytes. Cellular Signalling 2012;24(9):1863–71 doi 10.1016/j.cellsig.2012.05.001. [PubMed: 22588126]
39. Itoh Y, Sanosaka M, Fuchino H, Yahara Y, Kumagai A, Takemoto D, et al. Salt-inducible Kinase 3 Signaling Is Important for the Gluconeogenic Programs in Mouse Hepatocytes *. Journal of Biological Chemistry 2015;290(29):17879–93 doi 10.1074/jbc.M115.640821. [PubMed: 26048985]
40. Roland BP, Amrich CG, Kammerer CJ, Stuchul KA, Larsen SB, Rode S, et al. Triosephosphate isomerase I170V alters catalytic site, enhances stability and induces pathology in a Drosophila model of TPI deficiency. Biochim Biophys Acta 2015;1852(1):61–9 doi 10.1016/j.bbadis.2014.10.010. [PubMed: 25463631]

41. Savitski MM, Reinhard FB, Franken H, Werner T, Savitski MF, Eberhard D, et al. Tracking cancer drugs in living cells by thermal profiling of the proteome. Science 2014;346(6205):1255784 doi 10.1126/science.1255784. [PubMed: 25278616]
42. Huang JX, Lee G, Cavanaugh KE, Chang JW, Gardel ML, Moellering RE. High throughput discovery of functional protein modifications by Hotspot Thermal Profiling. Nature Methods 2019;16(9):894–901 doi 10.1038/s41592-019-0499-3. [PubMed: 31384043]
43. Faubert B, Vincent EE, Griss T, Samborska B, Izreig S, Svensson RU, et al. Loss of the tumor suppressor LKB1 promotes metabolic reprogramming of cancer cells via HIF-1α. Proceedings of the National Academy of Sciences 2014;111(7):2554–9 doi 10.1073/pnas.1312570111.
44. Xu HG, Zhai YX, Chen J, Lu Y, Wang JW, Quan CS, et al. LKB1 reduces ROS-mediated cell damage via activation of p38. Oncogene 2015;34(29):3848–59 doi 10.1038/onc.2014.315. [PubMed: 25263448]
45. Li F, Han X, Li F, Wang R, Wang H, Gao Y, et al. LKB1 Inactivation Elicits a Redox Imbalance to Modulate Non-small Cell Lung Cancer Plasticity and Therapeutic Response. Cancer Cell 2015;27(5):698–711 doi 10.1016/j.ccell.2015.04.001. [PubMed: 25936644]
46. Kim J, Hu Z, Cai L, Li K, Choi E, Faubert B, et al. CPS1 maintains pyrimidine pools and DNA synthesis in KRAS/LKB1-mutant lung cancer cells. Nature 2017;546(7656):168–72 doi 10.1038/nature22359. [PubMed: 28538732]
47. Schachner LF, Soye BD, Ro S, Kenney GE, Ives AN, Su T, et al. Revving an Engine of Human Metabolism: Activity Enhancement of Triosephosphate Isomerase via Hemi-Phosphorylation. ACS Chemical Biology 2022;17(10):2769–80 doi 10.1021/acschembio.2c00324. [PubMed: 35951581]
48. Ji H, Ramsey MR, Hayes DN, Fan C, McNamara K, Kozlowski P, et al. LKB1 modulates lung cancer differentiation and metastasis. Nature 2007;448(7155):807–10 doi 10.1038/nature06030. [PubMed: 17676035]
49. Shackelford David B, Abt E, Gerken L, Vasquez Debbie S, Seki A, Leblanc M, et al. LKB1 Inactivation Dictates Therapeutic Response of Non-Small Cell Lung Cancer to the Metabolism Drug Phenformin. Cancer Cell 2013;23(2):143–58 doi 10.1016/j.ccr.2012.12.008. [PubMed: 23352126]
50. Svensson RU, Parker SJ, Eichner LJ, Kolar MJ, Wallace M, Brun SN, et al. Inhibition of acetyl-CoA carboxylase suppresses fatty acid synthesis and tumor growth of non-small-cell lung cancer in preclinical models. Nature Medicine 2016;22(10):1108–19 doi 10.1038/nm.4181.
51. Deng J, Thennavan A, Dolgalev I, Chen T, Li J, Marzio A, et al. ULK1 inhibition overcomes compromised antigen presentation and restores antitumor immunity in LKB1-mutant lung cancer. Nature Cancer 2021;2(5):503–14 doi 10.1038/s43018-021-00208-6. [PubMed: 34142094]
52. DuPage M, Mazumdar C, Schmidt LM, Cheung AF, Jacks T. Expression of tumour-specific antigens underlies cancer immunoediting. Nature 2012;482(7385):405–9 doi 10.1038/nature10803. [PubMed: 22318517]
53. Ngo B, Kim E, Osorio-Vasquez V, Doll S, Bustraan S, Liang RJ, et al. Limited Environmental Serine and Glycine Confer Brain Metastasis Sensitivity to PHGDH Inhibition. Cancer Discovery 2020;10(9):1352–73 doi 10.1158/2159-8290.Cd-19-1228. [PubMed: 32571778]
54. Cheung EC, Ludwig RL, Vousden KH. Mitochondrial localization of TIGAR under hypoxia stimulates HK2 and lowers ROS and cell death. Proceedings of the National Academy of Sciences 2012;109(50):20491–6 doi doi:10.1073/pnas.1206530109.
55. Bensaad K, Cheung EC, Vousden KH. Modulation of intracellular ROS levels by TIGAR controls autophagy. The EMBO Journal 2009;28(19):3015–26 doi 10.1038/emboj.2009.242. [PubMed: 19713938]
56. Lee P, Vousden KH, Cheung EC. TIGAR, TIGAR, burning bright. Cancer & Metabolism 2014;2(1):1 doi 10.1186/2049-3002-2-1. [PubMed: 24383451]
57. DuPage M, Dooley AL, Jacks T. Conditional mouse lung cancer models using adenoviral or lentiviral delivery of Cre recombinase. Nature Protocols 2009;4(7):1064–72 doi 10.1038/nprot.2009.95. [PubMed: 19561589]

58. Rock JR, Randell SH, Hogan BLM. Airway basal stem cells: a perspective on their roles in epithelial homeostasis and remodeling. Disease Models & Mechanisms 2010;3(9-10):545–56 doi 10.1242/dmm.006031. [PubMed: 20699479]

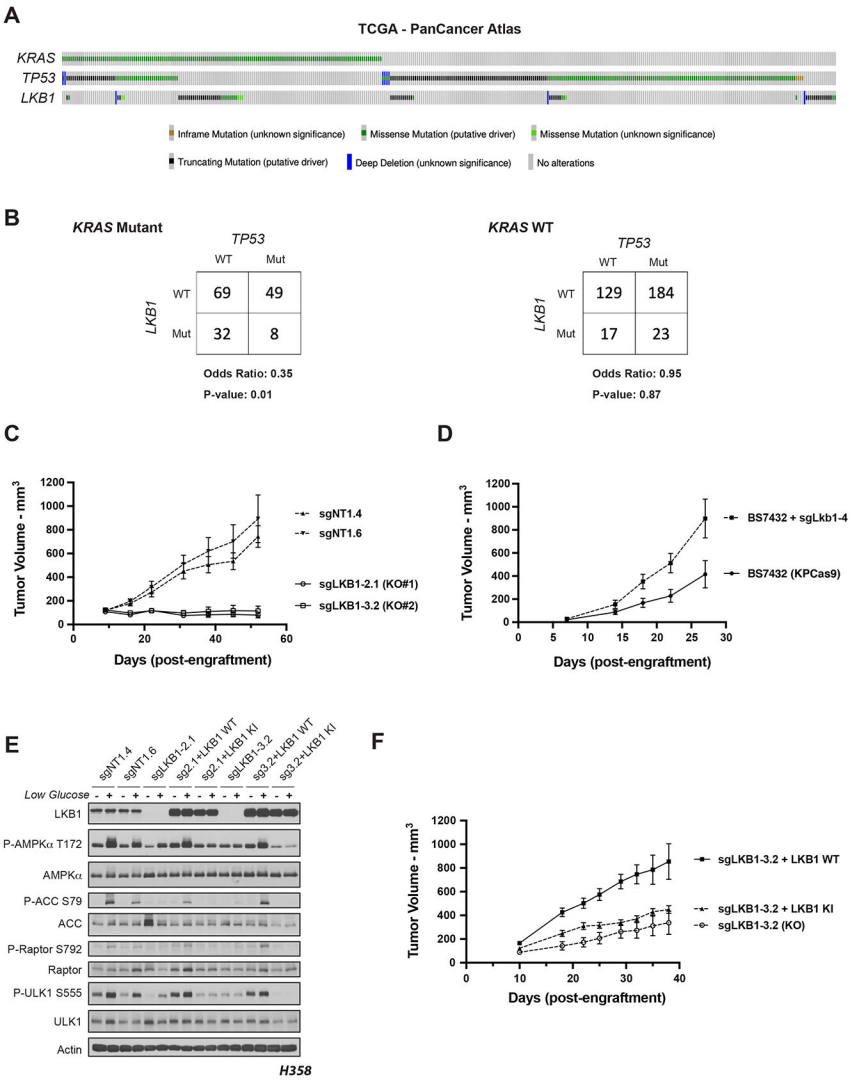

Figure 1. Co-occurrence of *KRAS*, *TP53* and *LKB1* mutations differentially affects growth of human and mouse LUADs.

(A) The Cancer Genome Atlas PanCancer Atlas oncoprint of co-occurrence of *KRAS*, *TP53* and *LKB1* in human lung adenocarcinoma patients. **(B)** Fisher's exact test of statistical likelihood of co-occurrence of *LKB1* and *TP53* mutations in a *KRAS* mutant or wildtype background respectively. **(C)** Graph of mean (+/− s.e.m.) tumor volumes of sub-cutaneous flank injections of H358 (*KRAS;TP53*) isogenic clones expressing Cas9 and a non-targeting (sgNT1.4 and sgNT1.6) or LKB1-specific (sgLKB1-2.1 and sgLKB13.2) guide RNA. 1 x 10^6 cells implanted in right hind flank (n = 10 per cohort). **(D)** Mean (−/+ s.e.m.) volumes of isogenic KPCas9 lung adenocarcinoma allograft tumors expressing a non-targeting (BS7432) or Lkb1-specific (sgLkb1-4) guide RNA. 0.25 x 10^6 cells implanted in left and right flank of C57Bl/6J mice (n = 10 per cohort). **(E)** Western blot analysis of H358 (*KRAS*;*TP53*) isogenic clones (KP: sgNT1.4 and sgNT1.6; KPL: sgLKB1-2.1 and sgLKB1-3.2) and KPL lines with additional transgenic expression of guide RNA resistant LKB1 wildtype (WT) (sgLKB1-2.1 + LKB1 WT and sgLKB1-3.2 + LKB1 WT) or LKB1 kinase inactive (KI) (sgLKB1-2.1 + LKB1 KI and sgLKB1-3.2 LKB1 KI) and treated with

11.1 mM or 0.5 mM glucose for 6 hours as indicated. Restoration of AMPK signaling in LKB1 WT lines in response to 0.5 mM glucose validated by blotting for P-AMPK Thr172 and downstream substrates (P-ACC S79, P-ULK1 S555, P-Raptor S792). Similar results observed in three independent experiments and in an additional *KRAS*;*TP53* cell line, H2009 (Figure S1E). **(F)** Graph of mean (−/+ s.e.m.) tumor volumes of sub-cutaneous flank injections of H358 (*KRAS;TP53*) isogenic clones with transgenic expression of an empty vector (KO) or guide RNA resistant LKB1 wildtype (LKB1 WT) or LKB1 kinase inactive (LKB1 KI). 1 x 10^6 cells implanted in right hind flank (n = 10 per cohort).

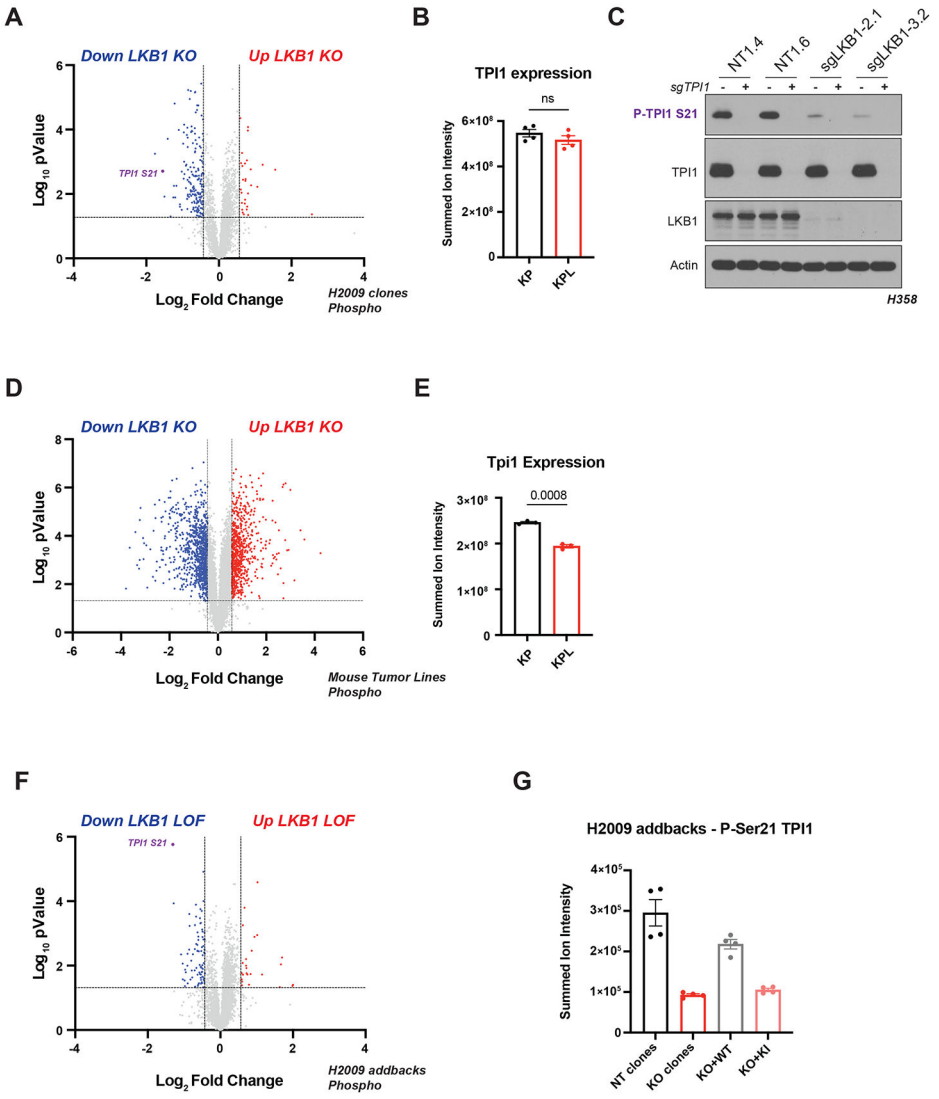

Figure 2. Phosphorylation of human TPI1 is LKB1-dependent and regulates triose phosphate levels.

(A) Volcano plot of quantitative phospho-proteomic data of genetic sensitivity in H2009 clones (2 KP clones and 2 KPL clones), two biological replicates each, N = 4 per genotype. Cells grown in 0.5 mM glucose for 6 hours. Phospho-peptides that pass statistical criteria (p-value < 0.05) are highlighted in black, red and blue, peptides that do not satisfy this are colored grey. Phospho-peptides colored red satisfy a fold change > 1.5; colored blue, fold change < −1.5. TPI1 P-Ser21 peptide labeled in purple text. **(B)** Bar graph of summed ion intensities for TPI1 protein expression in H2009 isogenic lines (KP: sgNT1.1 and sgNT1.2; KPL: sgLKB1-3.1 and sgLKB1-3.7). Cell-lines treated with 0.5 mM glucose for 6 hr prior to collection. Data presented are representative of 4 independent biological experiments and reported as the mean (−/+s.e.m.). Statistical significance determined by two-tailed paired t-test. **(C)** Western blot analysis of H358 (*KRAS*;*TP53*) isogenic cell (KP: sgNT1.4 and sgNT1.6; KPL: sgLKB1-2.1 and sgLKB1-3.2) and KPL lines to validate phospho-specific antibody. **(D)** Volcano plot for comparison of quantitative phospho-proteomic data of genetic

sensitivity in mLUAD cell-lines, 634T (KP) and Lkb1-t2 (KPL) in biological triplicate for each condition. Analysis conducted on cells treated with 0.5mM glucose for 6 hours in culture. Statistical criteria and color scheme same as for other Volcano plots presented. **(E)** Bar graph of summed ion intensities for TPI1 protein expression in mLUAD lines from companion unenriched total proteomic analysis. Data presented are representative of 3 independent biological experiments and reported as the mean (−/+s.e.m.). Statistical significance determined by two-tailed paired t-test. **(F)** Volcano plot of quantitative phospho-proteomic data of genetic sensitivity in H2009 isogenic clones including clones with transgenic expression of guide RNA resistant wildtype (WT) or kinase inactive (KI) LKB1 in LKB1-specific knockouts (sgLKB1-3.1 and sgLKB1-3.7) from Figure S1E, 4 biological replicates each. LKB1 Loss-of-function (LOF) group consisted of merging LKB1 knockout lines (KPL: sgLKB1-3.1 and sgLKB1-3.7) with lines expressing guide RNA resistant LKB1 KI (KPL + LKB1 KI: sgLKB1-3.1 + LKB1 KI and sgLKB1-3.7 + LKB1 KI); and compared to H2009 lines containing non-targeting guide RNA (KP: sgNT1.1 and sgNT1.2) merged with LKB1 knockout lines expressing guide RNA resistant LKB1 WT (KPL + LKB1 WT: sgLKB1-3.1 + LKB1 WT and sgLKB1-3.7 + LKB1 WT) at the phospho-peptide level. Cells were grown in 0.5 mM glucose for 6 hours. Statistical criteria and color scheme same as for panel A . TPI1 P-Ser21 peptide labeled in purple text. **(G)** Summed ion intensity of the H2009 (*KRAS*;*TP53*) isogenic clones (KP: sgNT1.1 and sgNT1.2; KPL: sgLKB1-3.1 and sgLKB1-3.7) and lines with additional transgenic expression of guide RNA resistant LKB1 wildtype (WT) (sgLKB1-3.1 + LKB1 WT and sgLKB1-3.7 + LKB1 WT) or LKB1 kinase inactive (KI) (sgLKB1-3.1 + LKB1 KI and sgLKB1-3.7 LKB1 KI) for the phospho-peptide containing Serine 21 of TPI1 from the experiments from which the volcano plot in Figure S2E was derived. Bar graph depicts each genotype individually and shows restoration of TPI1 phosphorylation in KPL lines expressing transgenic WT LKB1 but not KI LKB1. Ion intensities were normalized to identified TPI1 protein expression from paired unenriched total proteomic analysis across conditions to control for protein expression; the relevant phospho-peptide was observed 3 times in each biological replicate.

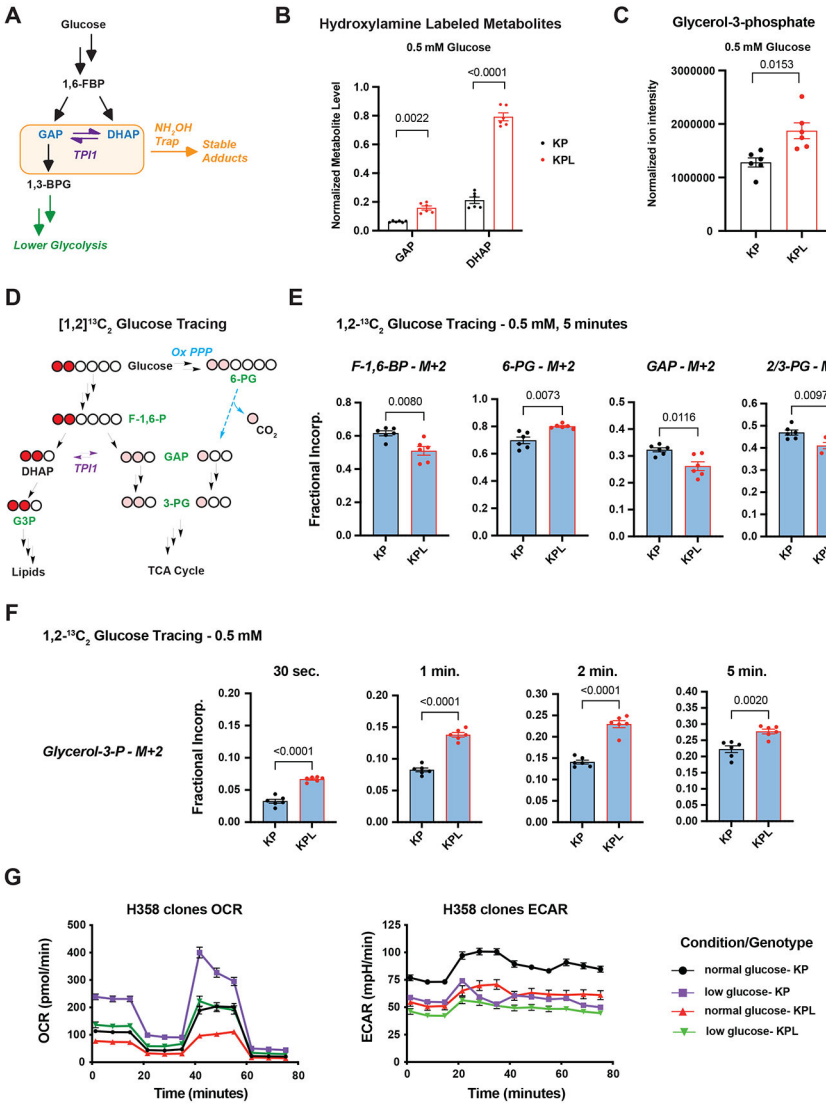

Figure 3. TPI1 phosphorylation regulates triose phosphate levels and metabolic flux.

(A) Schematic showing metabolites (shaded in the orange box) chemically labeled to create stable adducts. **(B)** Bar graph depicting *In-situ* chemical trapping metabolomics of hydroxylamine-labeled GAP and DHAP in H2009 clones (KP: sgNT1.1 and sgNT1.2; KPL: sgLKB1-3.1 and sgLKB1-3.7) treated in culture for 6 hours with 0.5 mM respectively. Data presented are representative of three independent biological experiments each containing three technical replicates and reported as the mean (−/+s.e.m.). Cell number normalized across models 12 hours prior to assay and samples normalized to an exogenous standard, d_3-serine. Statistical significance determined by two-tailed paired t-test. **(C)** Normalized ion intensity of glycerol-3-phosphate from steady-state analysis of H2009 clones treated for 30 minutes with 0.5 mM glucose. Analysis conducted in H2009 isogenic clones (KP: sgNT1.1 and sgNT1.2; KPL: sgLKB1-3.1 and sgLKB1-3.7) in biological triplicate and reported as the mean (−/+s.e.m.). Statistical significance determined by two-tailed paired t-test. **(D)** Schematic showing isotopic glucose tracing using positionally labeled 1,2-$^{13}C_2$ glucose with circles representing carbons in each metabolite. Red circles indicate isotopic

carbons and direct path to lipid synthesis through DHAP. Pink circles indicate readout of TPI1 conversion of DHAP to GAP and downstream glycolytic intermediates as well as alternate flux through oxidative pentose phosphate pathway. Green text indicates metabolites monitored and presented in histograms. **(E)** Isotopic tracing results for M+2 isotopologues at 5 minute time point. Analysis conducted in H358 isogenic lines (KP: sgNT1.4 and sgNT1.6; KPL: sgLKB1-2.1 and sgLKB1-3.2) in biological triplicate (N=6 per genotype) and reported as the mean (−/+s.e.m.). Statistical significance determined by two-tailed paired t-test. **(F)** Isotopic tracing results for M+2 isotopologue for Glycerol-3-phosphate at 30 seconds, 1, 2 and 5 minutes. Analysis conducted in H358 isogenic lines (KP: sgNT1.4 and sgNT1.6; KPL: sgLKB1-2.1 and sgLKB1-3.2) in biological triplicate (N=6 per genotype) and reported as the mean (−/+s.e.m.). Statistical significance determined by two-tailed paired t-test. **(G)** Mitochondrial Stress test results; Oxygen Consumption Rate (OCR) and Extracellular Acidification Rate (ECAR) plotted over the course of the assay. Analysis conducted in H358 isogenic lines (KP: sgNT1.4 and sgNT1.6; KPL: sgLKB1-2.1 and sgLKB1-3.2) in biological triplicate (N=6 per genotype) and reported as the mean (−/+s.e.m.) and treated as indicated with normal (11.1 mM) or low (0.5 mM) glucose for 6 hr prior.

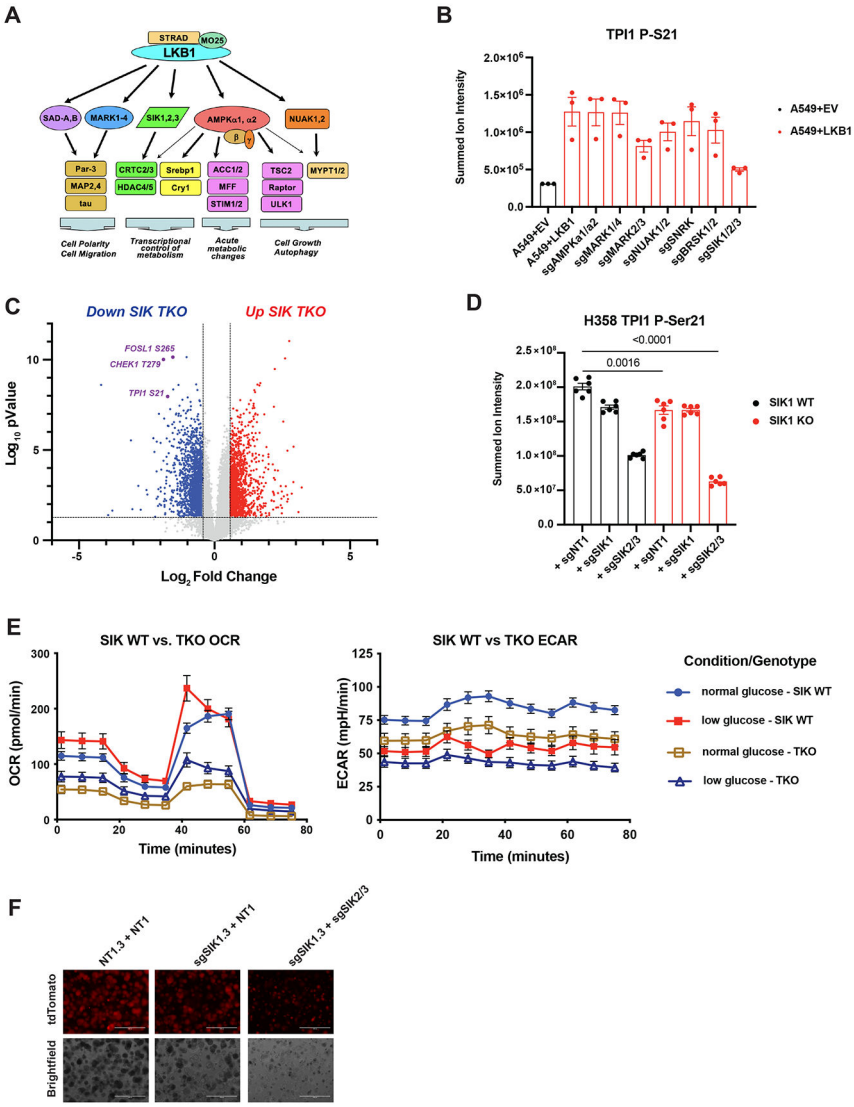

Figure 4. Salt Inducible Kinases phosphorylate human TPI1 in KP hLUAD cell lines.

(A) Cartoon depicting regulation of the AMPK-related (AMPKR) kinase family members by LKB1 and their downstream substrates. **(B)** Bar graph of summed ion intensity for the TPI1-derived Ser-21 phospho-peptide from extracts of A549 cell-lines infected with an empty vector or a vector expressing wild type LKB1; the indicated guide RNAs were used to inactivate members of the AMPKR subfamilies in LKB1 transgenic expressing cells. Cell lines were cultured in 11.1 mM glucose prior to analysis. Ion intensities were normalized to identified non-phosphorylated peptides across conditions to control for protein expression and reported as the mean (−/+ s.e.m.). **(C)** Volcano plot of quantitative phospho-proteomic data used to compare phosphorylation in H358 clones (2 KP clones and 2 KP SIK TKO clones, with 3 biological replicates of each). Cells were cultured in 0.5 mM glucose for 6 hours before lysis. Phospho-peptides that pass statistical criteria (p-value <0.05) are highlighted in black, red and blue; those that do not satisfy this criterion are colored grey. Proteins highlighted in red satisfy the fold change threshold (>1.5) after triple deletion of SIK1,2,3. Phospho-peptides highlighted in blue satisfy the fold change threshold

of < −1.5) for a decrease after SIK1,2,3 triple deletion. **(D)** Bar graph of summed ion intensities for the TPI1-derived, Ser-21 phospho-peptide in extracts of isogenic H358 cell-lines containing a non-targeting control (sgNT1.3 and sgNT1.4) or SIK1 specific (sgSIK1.3 and sgSIK1.4) guide RNA and additional control (NT1) SIK1 (sgSIK1) or dual SIK2 and SIK3 (sgSIK2/3) guide RNAs in a polyclonal population. Ion intensities were normalized against identified non-phosphorylated variant across conditions. Cell lines were cultured in 0.5 mM glucose prior to lysis, analyzed in biological triplicate per clone, N=6 per genotype and reported as the mean (−/+ s.e.m.). Statistical significance determined by two-tailed paired t-test. **(E)** Mitochondrial Stress test results; Oxygen Consumption Rate (OCR) and Extracellular Acidification Rate (ECAR) plotted over the course of the assay respectively. Analysis conducted in H358 isogenic lines used for phospho-proteomic analysis in (D) in biological triplicate (N=6 per genotype) and reported as the mean (−/+s.e.m.) and treated as indicated with normal (11.1 mM) or low (0.5 mM) glucose for 6 hr prior. **(F)** 3D spheroid growth in Matrigel of isogenic clones of the H358 cell line labeled with a tdTomato fluorescent reporter and expressing CAS9 and non-targeting controls (sgNT1.3) or SIK1-specific (sgSIK1-2.3) guide RNAs guide RNA and additional control (NT1) or dual SIK2 and SIK3 (sgSIK2/3) guide RNAs in a polyclonal population. 5,000 cells were seeded into Matrigel and grown for 14 days, and media changed every 24 hours. Images taken on EVOS fluorescence microscope under 4x magnification and filter to resolve tdTomato signal intensity and brightfield.

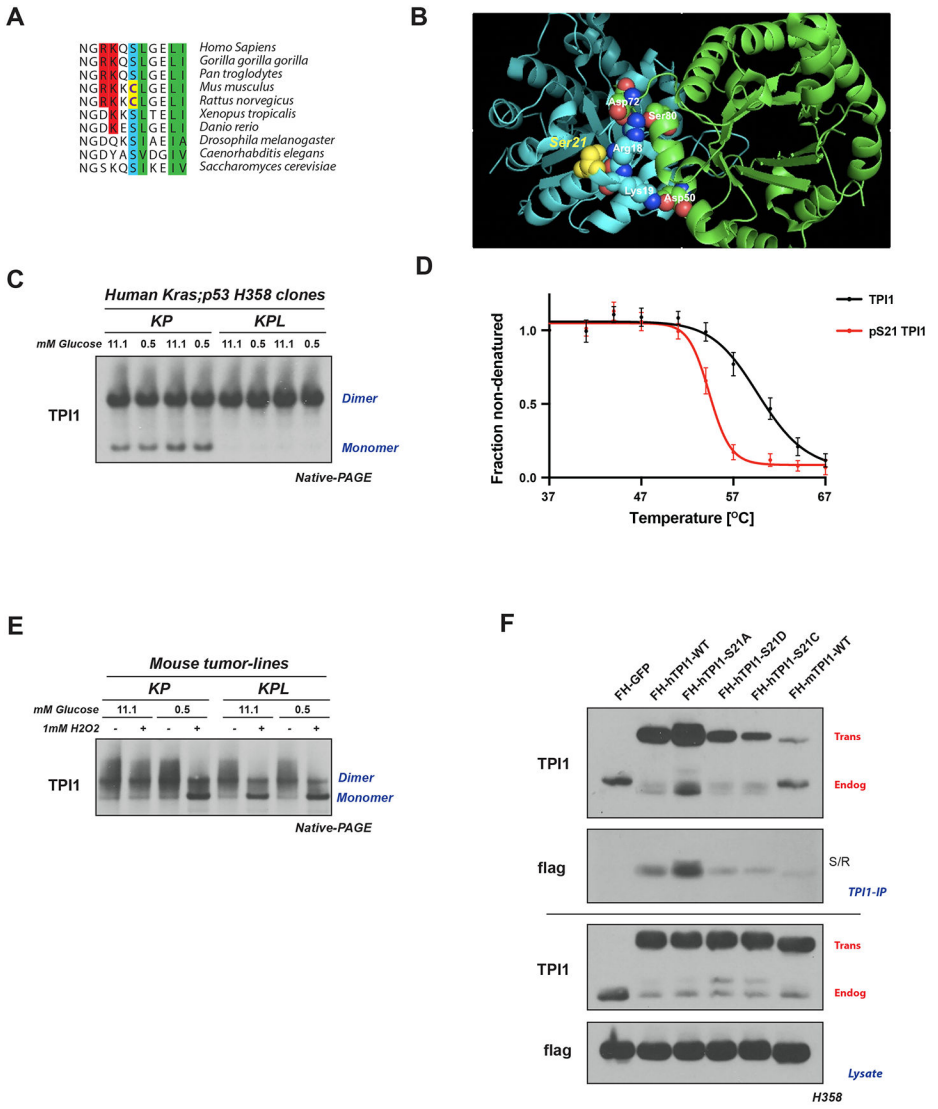

Figure 5. LKB1 regulates the multimeric state of hTPI1 but not mTpi1 due to an amino acid difference at position 21.

(A) Sequence alignment of TPI1 amino acid residues 16 to 26 across species, showing conservation of Ser21 from H. sapiens to *S. Cerevisiae*, with cysteine at position 21 in mouse and rat Tpi1. Cartoon comparing predicted side-chain chemistry, with oxidized cysteine and phosphorylated serine, is drawn below. **(B)** Crystal structure of TPI1 homodimer (cyan and green respectively) with critical residues highlighted in space-filling atoms. Serine 21 on the cyan monomer is highlighted in yellow. **(C)** Western blot analysis of Blue Native PAGE of human isogenic clones derived from KP H358 hLUAD cell-line. Cells were grown under normal (11.1 mM) or low (0.5 mM) glucose conditions for 6 hr prior to collection. **(D)** Melting curve plot from Thermal Profiling of unmodified and Serine 21 phosphorylated TPI1. Analysis conducted in H2009 and H358 isogenic clones expressing Cas9 and a non-targeting (sgNT1.1 and sgNT1.2 or sgNT1.4 and sgNT1.6, respectively) guide RNA. Data presented is from seven biological replicates and reported as the mean (−/+ S.D.) **(E)** Western blot (Blue Native PAGE) of extracts from mLUAD cell lines. Cells were

cultured in either 11.1 mM or 0.5 mM glucose for 6 hours then treated with 1 mM H_2O_2 for 15 minutes. **(F)** Western blot of proteins co-immunoprecipitated from extracts of H358 cells expressing Cas9 and a non-targeting (FH-GFP cell line) or TPI1-specific (all other cell lines) guide RNA and transgenic expression of Flag-HA tagged GFP or guide RNA resistant TPI1 allelic variants using a polyclonal antibody against full-length TPI1. Cells were cultured in 0.5 mM glucose for 6 hr prior to collection.

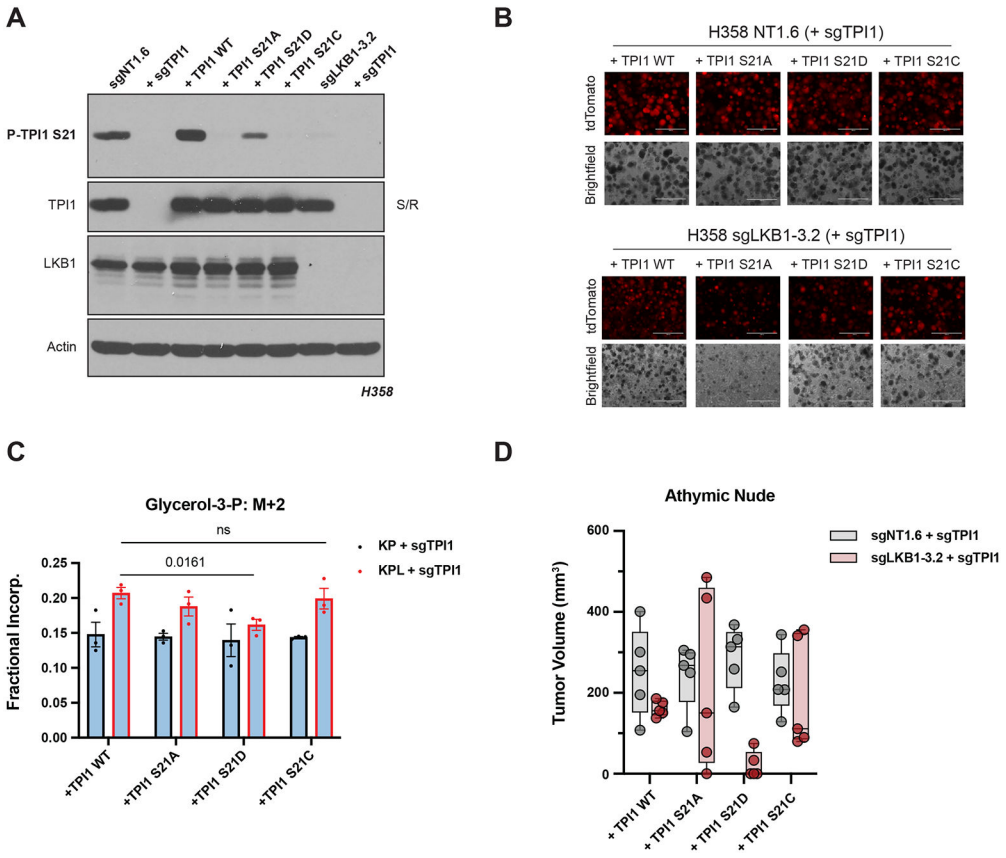

Figure 6. TPI1 amino acid differences at position 21 effect growth in organotypic culture, *in vivo*, and alter metabolic flux.

(A) Western blot analysis of human H358 (*KRAS*;*TP53*) isogenic KP and KPL cells (KP: sgNT1.6; KPL: sgLKB1-3.2) and derived untagged TPI1 allelic panel with phospho-specific antibody. **(B)** 3D spheroid growth in Matrigel of isogenic clones of the H358 cell line labeled with a tdTomato fluorescent reporter and expressing Cas9 and TPI1-specific (sgTPI1-3) guide RNA and transgenic expression of guide RNA resistant TPI1 allelic variants. 5,000 cells were seeded into Matrigel and grown for 14 days, and media changed every 24 hours. Images taken on EVOS fluorescence microscope under 4x magnification and filter to resolve tdTomato signal intensity and brightfield. **(C)** Isotopic tracing results for M+2 isotopologue for Glycerol-3-phosphate at 1 minute. Analysis conducted in H358 isogenic lines (KP: sgNT1.6; KPL: sgLKB1-3.2) with additional expression of sgTPI1 guide RNA and guide RNA resistant TPI1 allelic variants in biological triplicate (N=3 per genotype) and reported as the mean (−/+s.e.m.). Statistical significance determined by two-tailed paired t-test. **(D)** Subcutaneous tumor growth of human H358 isogenic lines (KP: sgNT1.6; KPL: sgLKB1-3.2) with additional expression of sgTPI1 guide RNA and guide RNA resistant TPI1 allelic variants. Cells first infected with control or LKB1 targeting guide RNA to produce isogenic KP and KPL respectively. Derived lines were then infected with lentiviruses encoding TPI1 sgRNA with subsequent lentiviral expression of transgenic guide RNA resistant hTPI1 WT, S21A or S21D and S21C and measured 30d following engraftment. Injections in athymic nude mice (n=5/group).

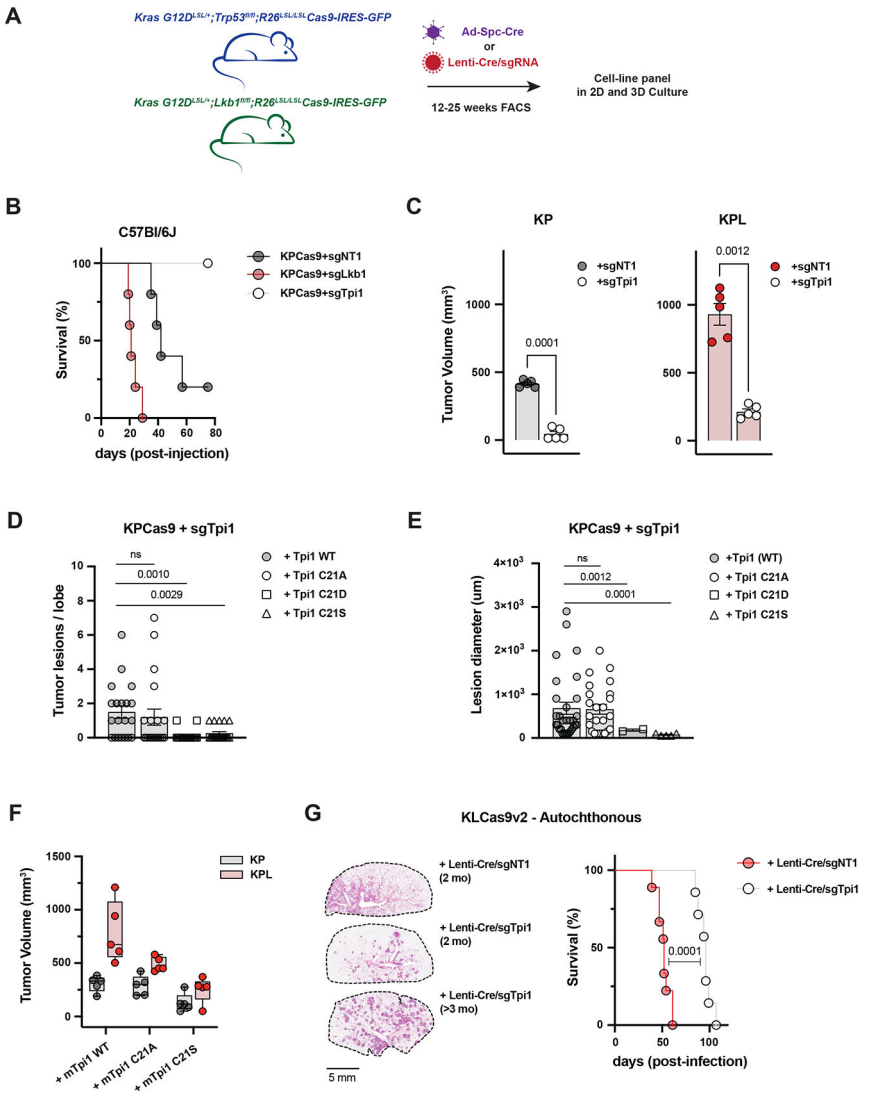

Figure 7. Tpi1 is required for tumor growth in KP and KPL LUAD models and humanizing TPi1 regresses tumor growth and burden.

(A) Cartoon schematic depicting generated conditional genetic mouse models and subsequent derived tumor derived cell lines. **(B)** C57Bl/6J mice survival following tail vein injection of KPCas9 cell line (BS7341) infected with lentiviruses encoding control or targeting sgRNAs (n=5/group). **(C)** Subcutaneous tumor growth of KP or KPL derived tumor cell lines (BS7432) infected with lentiviruses encoding control or targeting sgRNAs 30d following engraftment in C57Bl/6J mice (n=5/group); paired t-test provided above. **(D)** Histogram quantifying tumor lesions per lobe in tail vein injected KPcas9 (BS7431) Tpi1 allelic variants in C57Bl/6J mice (N=5/group) and reported as the mean (−/+ s.e.m.). Statistical significance determined by two-tailed paired t-test. **(E)** Histogram quantifying tumor lesion diameter in tail vein injected KPcas9 (BS7431) Tpi1 allelic variants in C57Bl/6J mice (N=5/group) and reported as the mean (−/+ s.e.m.). Statistical significance determined by two-tailed paired t-test. **(F)** Subcutaneous tumor growth of KPCas9 derived tumor cell line (BS7432) first infected with control or Lkb1 targeting guide RNA to produce

isogenic KP and KPL respectively. Derived lines were then infected with lentiviruses encoding Tpi1 sgRNA with subsequent lentiviral expression of transgenic guide RNA resistant mTpi1 WT, C21A or C21S and measured 30d following engraftment. Paired flank injections in C57Bl/6J mice were conducted (KP/KPL for each transgene) per mouse (n=5/group). **(G)** KLCas9v2 autochthonous tumor model survival following intratracheal administration of lentiviruses encoding cre-recombinase and control (sgNT) or targeting (sgTpi1) sgRNAs (n=12/group). Representative lung tumor burden in groups of mice at 8 weeks (sgNT and sgTpi1) and 14.5 weeks (sgTpi1) following intubation; histologic appearance of tumor lesions.